



HAL
open science

Linking Brain and Behavior States in Zebrafish Larvae Locomotion using Hidden Markov Models

Mattéo Dommanget-Kott, Jorge Fernandez-De-Cossio-Diaz, Monica Coraggioso, Volker Bormuth, Rémi Monasson, Georges Debrégeas, Simona Cocco

► **To cite this version:**

Mattéo Dommanget-Kott, Jorge Fernandez-De-Cossio-Diaz, Monica Coraggioso, Volker Bormuth, Rémi Monasson, et al.. Linking Brain and Behavior States in Zebrafish Larvae Locomotion using Hidden Markov Models. 2024. hal-04445557v2

HAL Id: hal-04445557

<https://hal.science/hal-04445557v2>

Preprint submitted on 22 Nov 2024

HAL is a multi-disciplinary open access archive for the deposit and dissemination of scientific research documents, whether they are published or not. The documents may come from teaching and research institutions in France or abroad, or from public or private research centers.

L'archive ouverte pluridisciplinaire **HAL**, est destinée au dépôt et à la diffusion de documents scientifiques de niveau recherche, publiés ou non, émanant des établissements d'enseignement et de recherche français ou étrangers, des laboratoires publics ou privés.



Distributed under a Creative Commons Attribution - NonCommercial 4.0 International License

Linking Brain and Behavior States in Zebrafish Larvae Locomotion using Hidden Markov Models

Mattéo Dommanget-Kott,^{1,2,*} Jorge Fernandez-de-Cossio-Diaz,^{3,4,*} Monica Coraggioso,¹ Volker Bormuth,¹ Rémi Monasson,³ Georges Debrégeas,^{1,†} and Simona Cocco^{3,‡}

¹*Institut de Biologie Paris-Seine (IBPS), Laboratoire Jean Perrin, Sorbonne Université, CNRS, France*

²*Université Paris Cité, France*

³*Laboratory of Physics of the Ecole Normale Supérieure,*

CNRS UMR 8023 PSL Research, Sorbonne Université, Université de Paris, France

⁴*Université Paris-Saclay, CNRS, CEA, Institut de Physique Théorique, 91191, Gif-sur-Yvette, France*

(Dated: November 22, 2024)

Understanding how collective neuronal activity in the brain orchestrates behavior is a central question in integrative neuroscience. Addressing this question requires models that can offer a unified interpretation of multimodal data. In this study, we jointly examine video-recordings of zebrafish larvae freely exploring their environment and calcium imaging of the Anterior Rhombencephalic Turning Region (ARTR) circuit, which is known to control swimming orientation, recorded *in vivo* under tethered conditions. We show that both behavioral and neural data can be accurately modeled using a Hidden Markov Model (HMM) with three hidden states. In the context of behavior, the hidden states correspond to leftward, rightward, and forward swimming. The HMM robustly captures the key statistical features of the swimming motion, including bout-type persistence and its dependence on bath temperature, while also revealing inter-individual phenotypic variability. For neural data, the three states correspond to left- and right-lateral activation of the ARTR circuit, known to govern the selection of left vs. right reorientation, and a balanced state, which likely corresponds to the behavioral forward state. To further unify the two analysis, we exploit the generative nature of the HMM, using the neural sequences to generate synthetic trajectories whose statistical properties are similar to the behavioral data. Overall, this work demonstrates how state-space models can be used to link neuronal and behavioral data, providing insights into the mechanisms of self-generated action.

Keywords: zebrafish; Hidden Markov Model; behavior; spontaneous neural activity; ARTR

I. INTRODUCTION

Animal behavior unfolds as a structured sequence of stereotyped motor actions, much like language. Understanding behavior thus requires identifying the vocabulary, *i.e.* the elementary behavioral units, and characterizing the corresponding grammar, *i.e.* their relative organization in time [1]. Uncovering this underlying structure is non-trivial. Over the last decade, numerous approaches have been proposed, building on the rapid development of data-driven computational methods. State-space models, in particular, appear to be well adapted, as they offer an unsupervised approach to sparse high-dimensional data into discrete states, while simultaneously unveiling their temporal structure. These include various implementations of Hidden Markov Models (HMMs) [2–5] and other statistical models [6–8].

Since behavior is driven by the brain activity, one expects the behavioral structure to be reflected in the spontaneous brain dynamics in the form of a sequence of discrete "brain states" - defined as metastable patterns of activity [9]. Neural activity can, as behavioral data, be

parsed to uncover neural states and their temporal sequences [10–12]. In general, however, behavioral or neuronal data are analyzed separately, as these experiments are typically conducted independently, limiting our ability to bridge the two processes. In contrast, a common modeling framework, when applied to both behavior and spontaneous neural activity, could help uncover a shared organizational structure linking self-generated neuronal dynamics and behavior.

Our model behavior is the spontaneous navigation of zebrafish larvae (see [8, 13–15]), which consists of discrete swimming bouts lasting ~ 100 ms and triggered at $\sim 1 - 2$ Hz. In previous studies the categorization of bouts was carried out independently of the examination of their temporal organization. In Marques *et al.* [16], the authors used PCA-based automatic segmentation to distinguish 13 different bout types, a number that they found sufficient to encompass the entire behavioral repertoire of the animal, including hunting, escape, social behavior, etc. However, in more constrained conditions when the fish merely explore its environment [17–23], a simple 3-state categorization is sufficient to describe their trajectories. In this case, the bouts are labeled as either forward, left-turn or right-turn based on the value of bout-induced body reorientation. The selection of these various bout types depends on sensory cues, resulting in the animal's capacity to ascend light [17, 20] or temperature [22, 24–26] gradients.

* These two authors contributed equally

† Correspondence: georges.debrégeas@sorbonne-universite.fr

‡ Correspondence: simona.cocco@phys.ens.fr

61 Importantly, the neural circuit that controls the
62 orientation of bouts has been identified as the anterior
63 rhombencephalic turning region (ARTR), a bilaterally
64 distributed circuit located in the anterior hindbrain.
65 Using combined calcium imaging and motor nerve
66 recordings, it was shown that the triggering of leftward
67 and rightward bouts are correlated with increased
68 activity on the corresponding side of the ARTR [18].

69
70 To characterize the behavioral and neural activities
71 and their possible relationship, we hereafter re-analyze
72 video recordings of freely swimming animals and ARTR
73 recordings, performed at various water temperature, us-
74 ing Hidden Markov Models (HMM). First, we show that
75 for the behavioral data, this approach provides an unbi-
76 ased and therefore more consistent method of bout-type
77 labeling compared to simple thresholding techniques as
78 used in earlier studies. We further use the HMM inferred
79 parameters to demonstrate and quantify inter-individual
80 variability in exploratory kinematics. We then apply a
81 similar 3-states HMM to the ARTR recordings performed
82 in paralyzed tethered fish, leading to the generation of
83 synthetic neuronal-based swimming sequences. Finally,
84 we compare the statistical structure of these synthetic
85 trajectories with real ones to assess the consistency of
86 the results across both behavioral and neural data.

87 II. RESULTS

88 A. Data

89 The behavioral data used in the present article comes
90 from a publication that examined the kinematic of free
91 exploration in zebrafish larvae [22]. The experimental de-
92 sign (Fig.1a) enables recording the trajectories of multi-
93 ple freely swimming larvae aged 5-7 days at temperatures
94 of 18°C, 22°C, 26°C, 30°C, and 33°C. At each tempera-
95 ture, the trajectories of multiple fish are combined into a
96 single dataset, and a set of kinematic parameters is ex-
97 tracted at each bout n , such as the angular change $\delta\theta_n$
98 in heading direction, the time elapsed since the previous
99 bout and the traveled distance (see Material and Meth-
100 ods sec. IV A). Water temperature was found to system-
101 atically impact the statistics of navigation, leading to
102 qualitatively different trajectories as illustrated in Fig-
103 ure 1b. As the temperature increases, trajectories tend
104 to become more winding and erratic. We have also re-
105 analyzed a second dataset of long-trajectories for 18 fish
106 tracked individually for over two hours at 26°C, in or-
107 der to assess inter-individual variability (see Material and
108 Methods sec. IV A).

109 The neural data comes from another publication in
110 which the spontaneous activity of the *Anterior Rhomben-*
111 *cephalic Turning Region* (ARTR) [27] (Fig.1e) was
112 recorded from 5-7 days old immobilized larvae express-
113 ing the calcium indicator GCaMP6f, using light-sheet
114 functional imaging. Several neural recordings (3-10) for

115 each one of the five temperatures (from 18°C to 33°C
116 (Fig.1b)) were analyzed. The fluorescence signal of each
117 neuron was further deconvolved to estimate an approxi-
118 mate spike train (see Material and Methods sec. IV B).

119 B. Modeling of behavior

120 1. Markov Models

121 The distribution of reorientation angles after each
122 bout, shown in Figure 1d, appears to be trimodal, sug-
123 gesting a classification of the bouts in 3 types: forward
124 (F), left-turn (L) and right-turn (R). In practice, this
125 categorization is generally carried out by thresholding
126 the distribution of re-orientation angles. Denoting the
127 state of swim bout n by s_n we have:

$$s_n = \begin{cases} R, & \text{if } \delta\theta_n < -\delta\theta_0 \\ F, & \text{if } -\delta\theta_0 < \delta\theta_n < +\delta\theta_0 \\ L, & \text{if } \delta\theta_n > +\delta\theta_0 \end{cases} \quad (1)$$

128 The use of the same threshold (in absolute value) to de-
129 tect left and right turns relies on the hypothesis that
130 zebrafish larvae, as a group, have no preferred direction
131 (*a.k.a.* non-handedness). As the exact value of $\delta\theta_0$ has
132 minimal qualitative impact on the results of the Markov
133 Chains, we adopt the same value $\delta\theta_0 = 10^\circ$ as in [22]; no-
134 tice that $\delta\theta_0$ is the same across all temperatures to avoid
135 introducing ad hoc, temperature-dependent biases. An
136 example of the classification of states along a swimming
137 trajectory is presented in Figure 2b.

138 Once the bout types are identified, we define a dy-
139 namical model for the trajectories $\dots \rightarrow s_{n-1} \rightarrow s_n \rightarrow$
140 $s_{n+1} \rightarrow \dots$ using a three-states Markov Chain (MC). In-
141 formally, the sequence of states (associated with the 3
142 different bout types) is described by the probabilistic au-
143 tomaton in Figure S3a. In this model, after each bout
144 n , a new state s_{n+1} is drawn randomly, conditioned only
145 on s_n (and not on previous states). The transition prob-
146 abilities between states, $P(s = s_n \rightarrow s' = s_{n+1})$, are
147 estimated by counting the numbers $\#$ of occurrences of
148 the transitions $s \rightarrow s'$ along the trajectories:

$$P(s \rightarrow s') = \frac{\#(s \rightarrow s')}{\#(s \rightarrow F) + \#(s \rightarrow L) + \#(s \rightarrow R)} \quad (2)$$

149 with $s, s' \in \{F, L, R\}$.

150 The top right eigenvector of the 3×3 transition matrix
151 gives access to the stationary probabilities $P(s)$ of the 3
152 states. These probabilities are in excellent agreement
153 with the frequencies of states estimated through direct
154 counting (difference < 0.003 across all bout types and
155 temperatures).

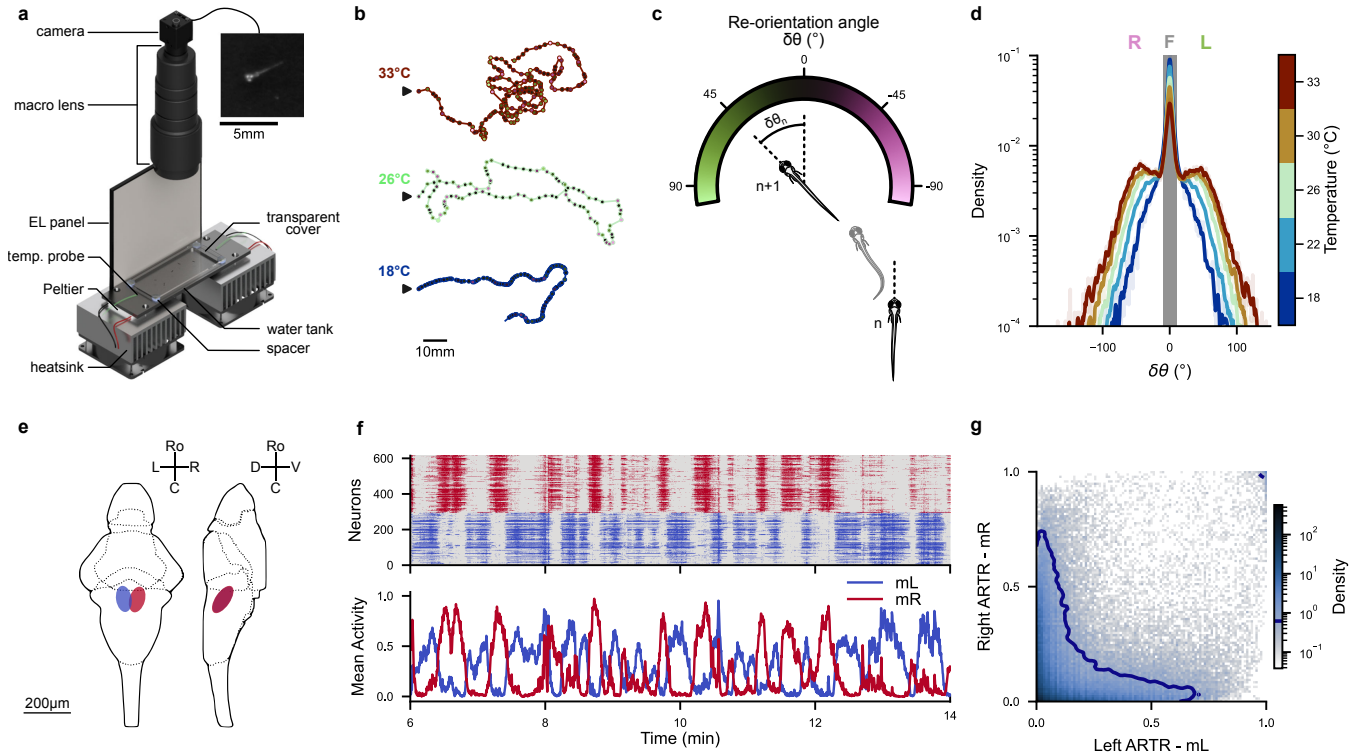


FIG. 1. **Behavioral and Neuronal Datasets:** (a) Overview of the experimental setup: Zebrafish larvae are free to move in a tank that is kept at a desired constant temperature by a Peltier module. An imaging system records images of the fish from above at a rate of 25 frames per second. The upper right panel provides a close-up view of a larva in a raw image. Adapted from Le Goc *et al.* [22]. (b) Example trajectories of zebrafish larvae in 2D space at various temperatures. Each point represents a swim bout, with the color indicating the corresponding re-orientation angle defined in panel c. The trajectories' starting points are denoted by black arrows. (c) Description of the convention used for the reorientation angle ($\delta\theta_n$) between two consecutive swim bouts (n and $n+1$). (d) Distribution of re-orientation angles ($\delta\theta_n$) for each ambient temperature. The grayed-out area corresponds to the re-orientation angles classified as forward bouts by thresholds at $\pm 10^\circ$. (e) Diagram of the *Anterior Rhombencephalic Turning Region* (ARTR) in larval zebrafish. Adapted from Wolf *et al.* [27]. (f) Example ARTR activity at 22°C . Top: Raster plot of neurons located in the left and right ARTR (blue and red respectively). Bottom: Mean activity m_L and m_R of neurons in the left and right ARTR. (g) Mean activities (m_L, m_R) of the ARTR for all recordings in the dataset. The blue contour line represents 90% of the joint distribution.

156

2. Hidden Markov Model

169

imposing that

$$\begin{aligned}
 P(F \rightarrow L) &= P(F \rightarrow R) \\
 P(L \rightarrow L) &= P(R \rightarrow R) \\
 P(L \rightarrow R) &= P(R \rightarrow L) \\
 P(L \rightarrow F) &= P(R \rightarrow F)
 \end{aligned}$$

We then turn to an agnostic categorization method, where states are inferred rather than *a priori* assigned. To do so, we consider a three-states Hidden Markov Model (HMM), see Figure 2a. Unlike MC, HMM makes a clear distinction between the observations (here the reorientation angles $\delta\theta_n$ treated as ‘symbols’) and the states of the system (here s_n , which are not directly accessible from the knowledge of $\delta\theta_n$, in contradistinction with the key assumption underlying MC). The HMM is defined by:

- The transition probabilities $P(s \rightarrow s')$ between the hidden states. We enforce the non-handedness by

This in turn ensures that steady state bout probability is left-right symmetric ($P(L) = P(R)$).

- The emission probabilities, $E(\delta\theta|s)$, relate the observations $\delta\theta$ to the hidden states s . For the forward state, we choose normally distributed reorientation angle emission distributions, centered in zero: $E(\delta\theta|F) = \mathcal{N}(\delta\theta; 0, \sigma)$. For turn states, we use Gamma distributed reorientation angles, with a positive or negative sign according to whether the state is Left or Right: $E(\delta\theta|L) = \Gamma(+\delta\theta; \alpha, \theta)$ and $E(\delta\theta|R) = \Gamma(-\delta\theta; \alpha, \theta)$, constraining $\alpha > 1$.

167
168162
163
164
165
166
167
168
169
170
171
172
173
174
175
176
177
178
179
180

Again, we ensured non-handedness by enforcing the same parameters for the left and right emission distribution. See Material and Methods sec. IV C for details about the validation of these emission distributions.

- A probability distribution for the initial state at the beginning of a trajectory.

We train HMM models for each dataset using the Baum-Welch algorithm, with a custom Julia [28, 29] implementation (available at <https://github.com/ZebrafishHMM2023/ZebrafishHMM2023.jl/tree/bioRxiv>).

C. State classification and behavioral persistence

1. Statistics of bout states

Since the Markov Chain inferred from thresholded data (MC, Fig.S3a) and the Hidden Markov Model (HMM, Fig.2a) share the same internal behavioral states, we can directly compare these two models and thus examine the impact of the labeling methods.

As illustrated with an example trajectory at 22°C in Figure 2b, MC and HMM labeling can differ significantly. MC-inferred sequences often exhibit multiple alternations between Forwards and Turns when the bouts reorientation angles are near the threshold, while for the same sequence, the HMM tends to consistently label these bouts as Turns. These differences result in a reclassification of approximately 60% of Forward bouts into Turning bouts at 22°C (Fig.S3e).

The HMM yields a relatively modest dependence of bout-type usage on temperature (see Fig.S3b). In contrast, the hard-threshold classification method used in MC lead to a systematic and pronounced increase in the fraction of turning bouts with rising temperature. This strong temperature dependence, previously reported in Le Goc *et al.* [22], may have thus been overestimated, as it partly reflects the ad-hoc assumption of a fixed (temperature-independent) threshold $\delta\theta_0$. Conversely, the HMM approach infers a gradual widening of the forward bouts angular distribution with increasing temperature that effectively corresponds to an increase in the angular threshold (see Fig.S2c-e).

2. Bout streaks and persistence

We further assessed how bout-type persistence, defined as the tendency to execute similar bouts in succession, depends on the chosen classification model. We start by describing trajectories as a series of streaks of similar bouts (forward, leftward or rightward), and then characterize the streak length distribution. For all bout types and models, the probability of observing a streak

of ℓ consecutive bouts of the same type decays exponentially, $P(\ell) \propto e^{-\ell/\ell_1}$, with ℓ_1 defining the characteristic streak length (Fig.2c). For turning bouts, we found $\ell_1^{\text{HMM}} \approx 1.4$ bouts while $\ell_1^{\text{MC}} \approx 0.9$ bouts at 22°C. Compared to MC, HMM-based labeling thus yield much longer turning streaks. In contrast, we find no significant difference in characteristic forward-streak length between HMM and MC. As temperature increases, we observe for both models that the characteristic streak length decreases (particularly for forward bouts, see Fig.1b).

Within the Markov or Hidden Markov Model frameworks, the average length $\ell_1(s)$ of a streak of bouts of type s is related to the probability $P(s \rightarrow s)$ of remaining in the same state through the simple relation $\ell_1(s) = -1/\ln P(s \rightarrow s)$. To distinguish the effects on bout-type persistence due to the presence of memory from the mere consequences of single-state frequencies, we introduce a null model, in which the transition probabilities are simply given by these frequencies, *i.e.* $P(s \rightarrow s') = P(s')$. In this null model without any memory, the average length of type- s bouts is simply $\ell_0(s) = -1/\ln P(s)$. The ratio $\ell_1(s)/\ell_0(s)$ is an estimator of the (relative) contribution of behavioral memory to bout-type persistence.

Results for this memory-induced persistence are shown in Figure 2d for the Markov (MC) and Hidden Markov (HMM) Models. The MC and HMM methods yield comparable outcomes for turning bouts at low temperature. However, HMM-based analysis further reveals a persistence for forward bouts at lower temperatures (Fig.2d), while this effect is absent in the MC model. Here again, this absence of forward persistence, previously reported in Karpenko *et al.* [20], is likely due to the mis-labeling associated with the hard-threshold method. Interestingly, such persistence effects vanish at higher temperatures, where the transition matrix becomes uniform (Fig.S3c,d), and all bouts become equiprobable ($P(F) \approx P(L) \approx P(R)$). One thus expect more erratic trajectories at higher temperatures, which is consistent with our observations (see Fig.1b).

3. Consistency of the MC and HMM descriptions of behavior

Taken together, the results above suggest that the Hidden Markov Model better captures persistence in reorientation by labeling bouts with small reorientation angles based on context. This leads to a more flexible and thus stable classification than the hard-thresholding method. However, given the absence of a ground truth, it remains unclear whether the labeling produced by the Hidden Markov Models is more accurate than the one produced by the standard threshold-based approaches.

One way to address this question is to examine to what extent each of these methods are self-consistent, *i.e.* guarantees that the inferred labeled sequences are

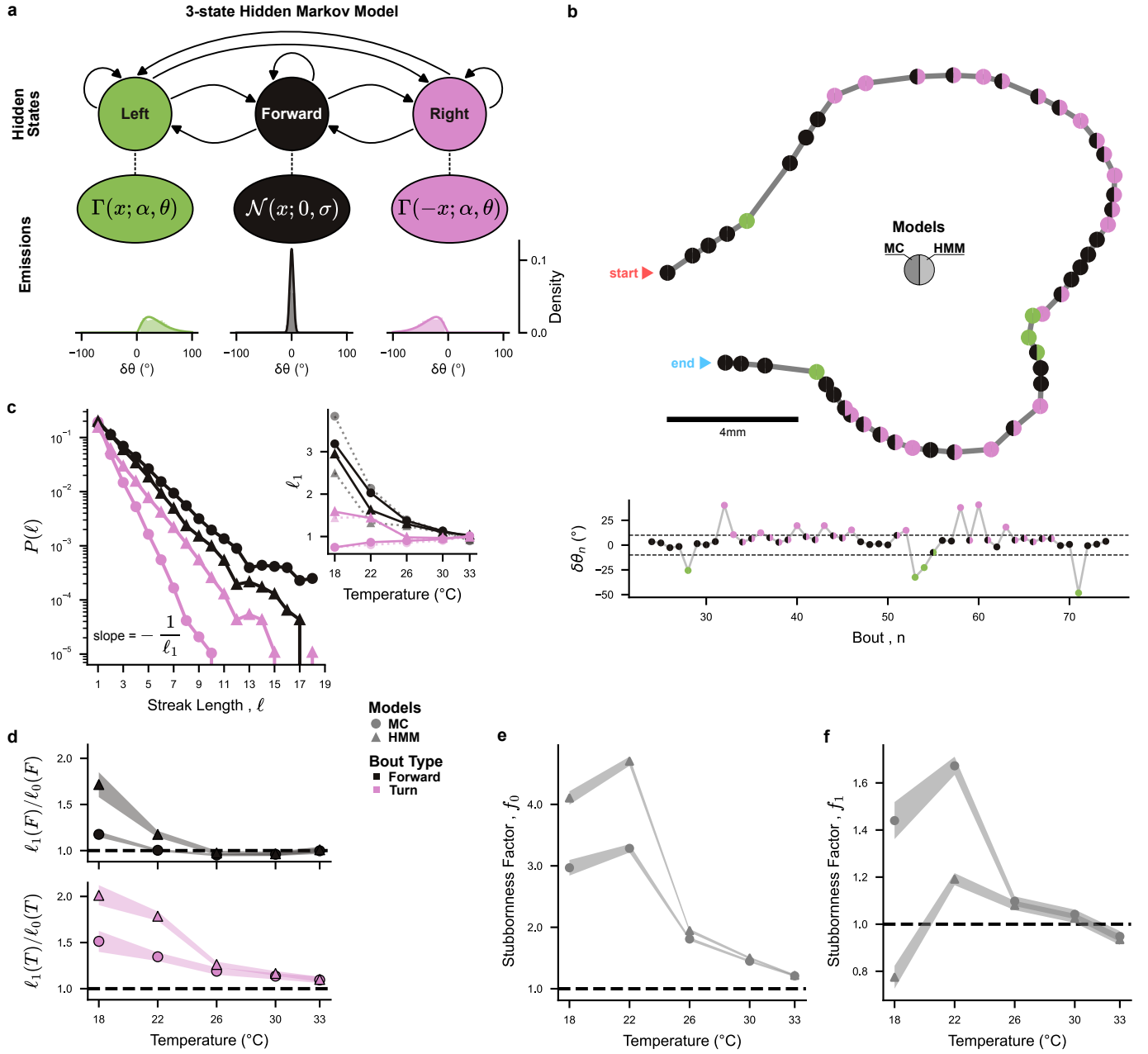


FIG. 2. 3-state Markov Chain and Hidden Markov Model - Memory effects emerge from better labeling: (a) Diagram illustrating the 3-state Hidden Markov Model (HMM) with emissions modeled as a normal distribution for Forward bouts, and gamma distributions for Turning bouts. Example emission distributions were taken at 26°C. (b) Differences in labeling between Markov Chain (MC) and HMM for an example trajectory at 22°C. Each point represents a swim bout, with the left color corresponding to the labeling according to the manual threshold used in MC, and right color indicating the HMM labeling using the Viterbi algorithm. Top: Trajectory in 2D space. Bottom: Evolution of the reorientation angle $\delta\theta_n$ for this trajectory, with the dashed lines representing the threshold $\delta\theta_0 = \pm 10^\circ$. (c) Probability $P(\ell)$ of observing a streak of ℓ consecutive forward bouts (black) or ℓ consecutive turning bouts in the same direction (pink), for MC (circles) and HMM (triangles), measured from data at 22°C. Inset: Temperature dependence of the persistence length characteristic length (ℓ_1). Dotted line: theoretical persistence length computed from the transition matrix, $\ell_1(s) = -1/\ln(P(s \rightarrow s))$. (d) Ratio of the observed persistence length ℓ_1 and the persistence expected in a no-memory null model, ℓ_0 vs. temperature. Forward bouts: $s = F$, black; turning bouts: $s \in L, R$, pink. (e) Temperature dependence of the stubbornness factor at $q = 0$ intermediary Forward bouts ($f_0 = \frac{P(L \rightarrow L) + P(R \rightarrow R)}{P(L \rightarrow R) + P(R \rightarrow L)}$). This factor is interpreted as a measurement of directional persistence during sequences of turning bouts. (f) Temperature dependence of the stubbornness factor at $q = 1$ intermediary Forward bouts ($f_1 = \frac{P(L \rightarrow F \rightarrow L) + P(R \rightarrow F \rightarrow R)}{P(L \rightarrow F \rightarrow R) + P(R \rightarrow F \rightarrow L)}$). This factor is interpreted as a measurement of directional memory after one forward bout, which for a 3-state model is a second order non-Markovianity. (e-f) The width of the shaded curves represent the estimated error in stubbornness factor from aggregated fish data (see Materials and Methods IVD).

truly markovian such that the bout type at a given time only depends on the type of the preceding bout. It has been previously noted that the hard-thresholding methods lead to significant non-markovianity. In particular, in a transition $T_1 \rightarrow F \rightarrow T_2$ with $T_1, T_2 \in \{L, R\}$, the two turning bouts tend to have the same orientation ($T_1 = T_2$). This means that the memory of orientation T_1 is maintained during the forward bout, in violation of the Markovian assumption. This observation led to propose a 4-state Markov system comprising two independent Markov chains, independently controlling the forward-turn bout transitions, and directional left-right bout transitions (see Fig.S4b for a diagram of this 4-state model) [20, 22].

Given that our 3-state Hidden Markov Model (HMM) re-labels numerous Forward bouts as Turn bouts, we ask whether this new classification might alleviate this non-Markovianity issue, such that the ad hoc 4-state model might no longer be needed. We thus propose a new test of Markovian violation specifically designed for our use case, that we apply to both the HMM and MC models.

We introduce the *stubbornness factor* f_q to empirically assess the tendency of larvae to retain their orientation after a sequence of q intermediary forward bouts (Fig.S4b, Materials and Methods sec. IV D):

$$f_q = \frac{P(T_1 \rightarrow F^q \rightarrow T_2 | T_1 = T_2)}{P(T_1 \rightarrow F^q \rightarrow T_2 | T_1 \neq T_2)} \quad (3)$$

with $T_1, T_2 \in \{L, R\}$ and $F^q = \underbrace{F \rightarrow F \rightarrow \dots \rightarrow F}_q$.

Owing to the loss of orientational memory after a forward bout, a non-handed 3-state Markovian model should have $f_q = 1$ for $q \geq 1$ (Materials and Methods sec. IV E). On the other hand, $f_{q=0}$ is a measurement of directional persistence during uninterrupted sequences of turning bouts.

We found that most of the memory effects captured by the HMM occur at $q = 0$, and that the *stubbornness* reaches $f_q \approx 1$ for $q \geq 1$, suggesting that the HMM-inferred bout sequences are quasi-markovian. In comparison, and for lower temperatures, the thresholded MC classification displays lower persistence at $q = 0$ but higher *stubbornness* at $q = 1$ as seen on Figure 2e-f (and less significantly at $q = 2$, see Fig.S4d). This suggests that the thresholded labeling leads to Markov violation primarily due to the mislabeling of turn bouts as forward bouts during turning streaks, as anticipated in the previous section and illustrated on Figure 2b. As this *stubbornness* is mostly significant at $q = 1$, we expect that most mislabelings are one-off errors.

In summary, previous works using an ad hoc threshold to classify bouts had dismissed 3-states Markov models because the resulting sequences were non-markovian. We found that by using an unsupervised method to simultaneously label the data and infer a Markov Model, we could unveil previously underestimated memory effects in zebrafish reorientation statistics. Our results suggest that the apparent non-markovianity reported in previous

studies was mainly caused by the mislabeling of turning bouts as forward bouts during sequences of consecutive turns. The HMM seems to be a clear improvement, identifying quasi-Markovian 3-state sequences and providing a more robust representation of the swimming dynamics.

D. Behavioral phenotyping from long individual fish trajectories

As HMM provides an unbiased quantification of the behavior, we now ask whether the approach is accurate enough to detect behavioral differences between specimen (inter-individual variability) and whether it can enable the unambiguous identification of each animal.

In the preceding sections, the dataset used to infer the models comprised trajectories from multiple fish, as the different individuals swimming together during a given assay could not be distinguished. To address the question of individuality, we used additional experiments reported in Le Goc *et al.* [22], in which individual fish were tracked at 26°C (see Materials and Methods IV A). A total of 18 fish were recorded for over 2 hours.

We first split the 2h-long recorded sequence of each individual fish into smaller periods (chunks) of ≈ 12 minutes each, and trained an HMM on each of these chunks (see diagram in Figure 3a-b). For each fish, the parameters of these HMMs exhibit significant variability (as shown by the vertical error bars in Figure 3c). This variability between the different chunks reflects both intra-individual (temporal) variability and, to a lesser extent, inference uncertainty due to the limited sampling of the HMM (see Fig.S5). We then also trained a single HMM on the entire dataset of a single fish (the “global” HMM). Figure 3c compares selected parameters of the global HMM for each fish, against the average parameters over several HMMs trained on the chunk trajectories (see Fig.S5 for all parameters). There is a clear trend between the global HMM and the average behavior of the chunk HMMs. Therefore, although a fish exhibits variability during a long sequence of bouts, the variability between distinct fish is larger.

These results suggest that the HMM models can be used to distinguish different fish from observations of their bout sequences. To test this hypothesis, we split the trajectories of each fish into a training and a withheld test set. After training the HMM on the train set for a particular fish, we computed the likelihood of all fish trajectories in the test set, and compared them. For 14 out of the 18 fish, the test set that yield the maximum likelihood rightly identifies the fish used to train the HMM (Fig.3d). This finding suggests that the HMM captures behavioral parameters which are distinctive enough to discriminate between different fish. Given the large variability exhibited by a single fish, one expects this discriminative ability to increase with the duration of the training sequences. To quantify this, we further evaluated the likelihoods of subsets of the test fish trajectories, and

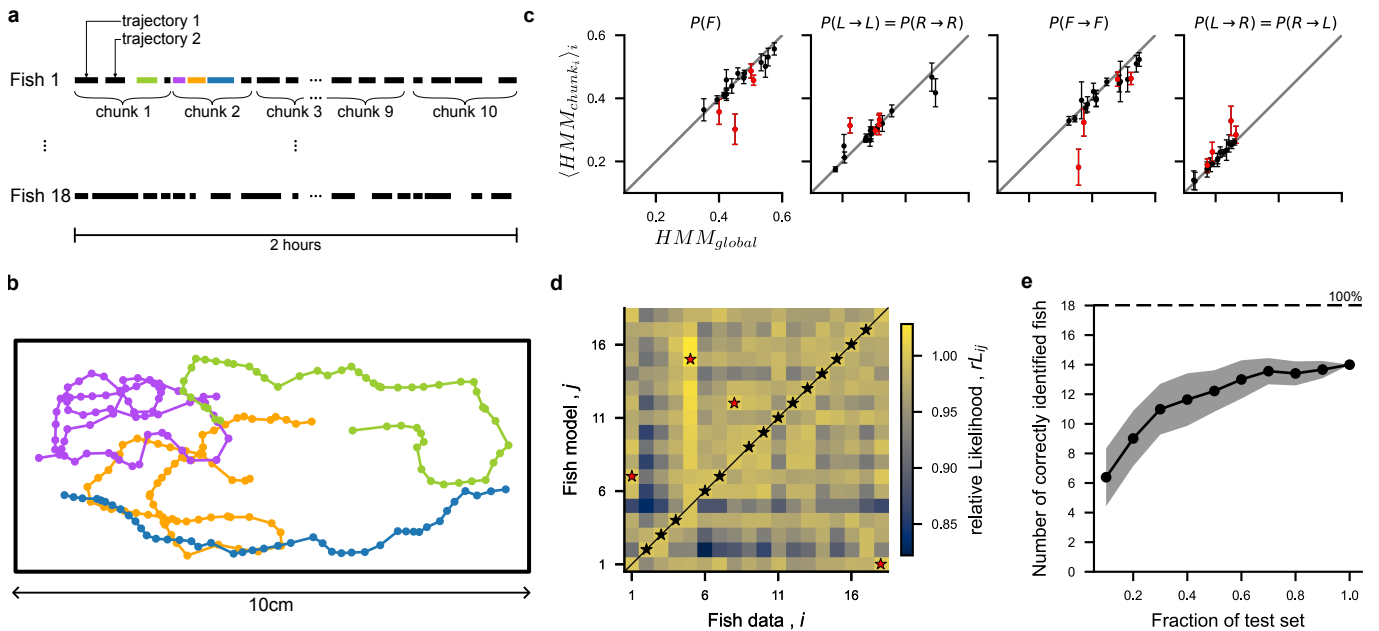


FIG. 3. **Fish identification from long trajectories:** (a) Diagram describing the dataset. Trajectories from 18 fish recorded over 2-hour sessions, were each split into 10 chunks (mean = 9.5 ± 0.5 trajectories per chunk) (b) Example trajectories for fish 1. (c) HMM parameters inferred from all the trajectories of a fish (referred to as global), compared with the HMM parameters trained on chunks of that fish’s trajectories. Only four HMM parameters are shown for clarity : the steady state probability of forward turns $P(F)$, the transition probabilities for forward-forward $P(F \rightarrow F)$, turn-turn in the same direction $P(T_1 \rightarrow T_2|T_1 = T_2)$, and turn-turn in opposite direction $P(T_1 \rightarrow T_2|T_1 \neq T_2)$ (see FigS5 for all parameters). Each dot represents a fish, and the error bars correspond to the standard error of the mean. Points labeled in red correspond to fish misidentified in panel d. (d) Confusion matrix between data coming from fish i and HMM trained on fish j . The relative likelihood $rL_{i,j} = \frac{L(data_i|model_j)}{L(data_i|model_i)}$ is used to evaluate which fish identity is most likely according to each model (indicated with black stars for correctly identified fish, and red stars for misidentification). (e) Number of correctly identified fish determined from model likelihood when only a fraction f of the test data is used for identification. The shaded area indicates the standard deviation across 100 trials. In each trial, the data trajectories of each fish were randomly split into train and test sets (50%).

395 recorded the number of times that the maximum likeli-
 396 hood HMM corresponded to the correct fish (Figure 3e)
 397 . Even when withholding 80% of the sequence, we were
 398 able to correctly identify 10 out of the 18 fish. These
 399 results suggest that individual fish exhibit variable but
 400 distinctive behavior which can be captured by the HMM.

401 E. Modeling of neural data

402 The selection of turning bouts orientation in zebrafish
 403 is known to be controlled by a small bilaterally dis-
 404 tributed circuit in the anterior hindbrain, called *Ante-*
 405 *rior Rhombencephalic Turning Region* (ARTR). This cir-
 406 cuit displays self-sustained alternating activity between
 407 its left- and right-lateral sub-population, with a period of
 408 the order of tens of seconds (Fig.1e). The animal tends to
 409 execute left turns when the left ARTR is active while the
 410 right ARTR is inactive (and vice versa for right turns)
 411 [18].

412 In contrast, no specific circuit has yet been identified
 413 for the selection of turn vs forward bouts. The hypoth-
 414 esis that two distinct circuits are involved in bout-type

415 selection is consistent with the 4 states Markovian model
 416 of navigation, in which two independent Markov chains
 417 drive the two selection processes. However, the 3-states
 418 Markovian model supported by the HMM analysis sug-
 419 gests that the same circuit (ARTR) could drive the se-
 420 lection of all 3 bout-types.

421 In order to test this hypothesis, we re-analyzed the
 422 ARTR recordings reported in Wolf *et al.* [27] using a 3-
 423 state HMM (Fig.4a). We posit an independent neural
 424 model for the activity of the N recorded neurons, yield-
 425 ing, for each state, the emission probability:

$$P(\sigma_1, \sigma_2, \dots, \sigma_N | s) = \prod_{i=1}^N \frac{e^{h_i^s \sigma_i}}{(1 + e^{h_i^s})} \quad (4)$$

426 where $(\sigma_1, \sigma_2, \dots, \sigma_N)$ is a neuronal configuration, s is
 427 the hidden state, and h_i^s is the local field representing
 428 the effective excitability of neuron i in state s . The
 429 model thus includes $3 \times N$ parameters h_i^s , associated
 430 to each neuron and each hidden states. Notice that for
 431 the neural HMM, the non-handedness of the behavioral
 432 HMM is not enforced.
 433

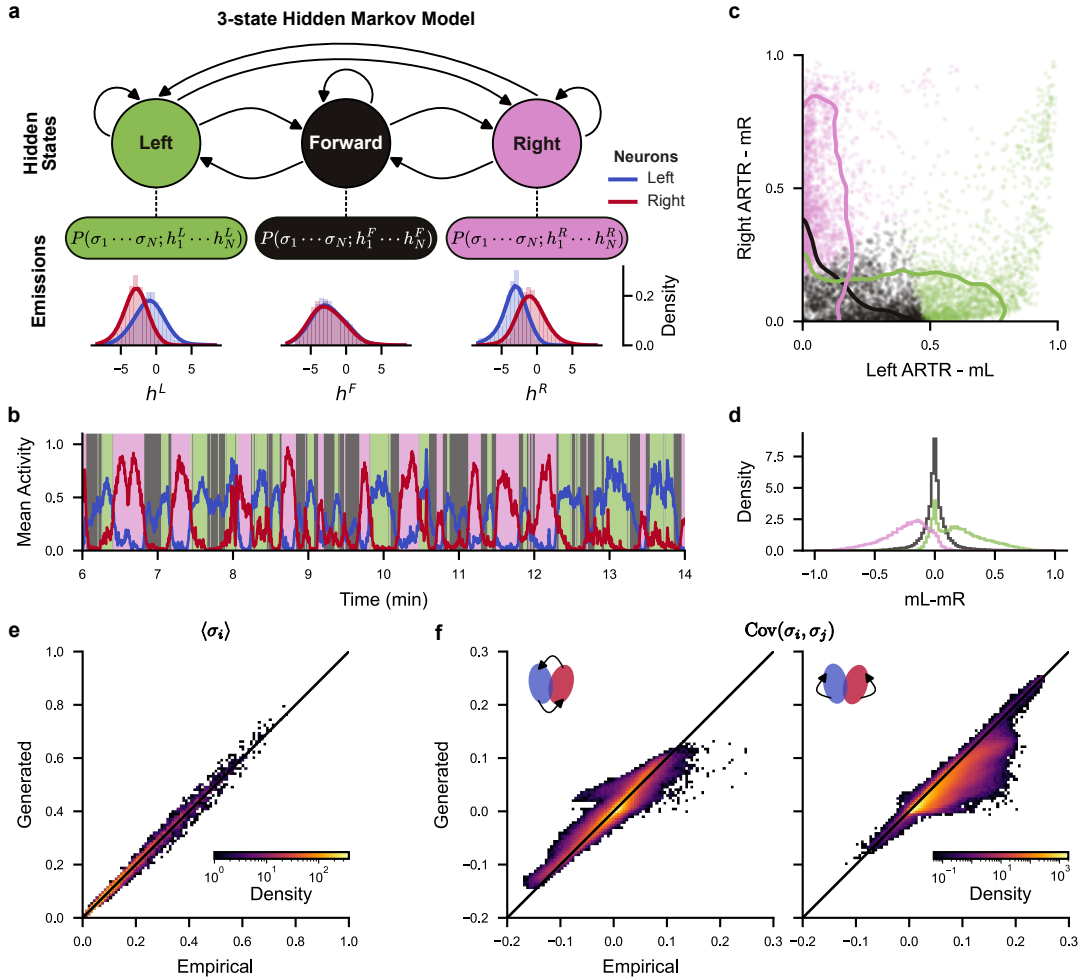


FIG. 4. **3-state Hidden Markov Model (HMM) describes ARTR neuronal statistics:** (a) Diagram illustrating the 3-state Hidden Markov Model (HMM) with emissions described as independent models of the ARTR neuronal population, see Eq. (4). Distributions of fields h_i^s are shown for all recorded fish for neurons in the left and right ARTR (in blue and red respectively). (b) Example ARTR activity (see Fig. 1f) classified with the 3-state HMM. Blue and red lines represent the mean activity of neurons in the left (m_L) and right (m_R) ARTR, respectively. (c) HMM classification in the (m_L, m_R) space. Dots represent neuronal configurations taken from the example recording in panel b. Solid lines represent 90% of the distributions for all recordings combined. (d) Distributions of $m_L - m_R$ for each hidden state and all recordings combined. e-f Comparison of empirical and HMM-generated neuronal statistics for all recordings combined. (e) Mean activity $\langle \sigma_i \rangle$ of neuron i . (f) Covariance $\text{Cov}(\sigma_i, \sigma_j)$ of neurons i and j on opposite sides (left plot) and on the same sides (right plot) of the ARTR.

434 The distribution of fields h_i^s for the 3 hidden states, 449
 435 shown in Fig.4a, are used to assign labels to the three 450
 436 states (see Materials and Methods IV F). Consistent with 451
 437 our current understanding of the ARTR function for turn 452
 438 selection, the state with large values of the fields on the 453
 439 left and smaller values of the fields on the contralateral 454
 440 side is labeled "left" (and vice versa for "right"). The 455
 441 third state exhibits similar distributions of fields for neu- 456
 442 rons on the left and right side of the ARTR, and is labeled 457
 443 forward in analogy with behavior. The ARTR activity is 458
 444 thus modeled as a sequence of left-right-forward states.

445 With this classification, the forward state corresponds 459
 446 to a low mean neuronal activity of both the left (m_L) and 460
 447 right (m_R) sides of the ARTR, while turning states are 461
 448 associated with large activity on the ipsilateral side of the 462

449 ARTR (left state : $m_L > m_R$, right state : $m_L < m_R$,
 450 see Fig.4b-d).

451 This model accurately captures the mean activity of 452
 452 each neuron (Fig.4f), as well as the pairwise correlations 453
 453 between contralateral neurons. However, ipsilateral 454
 454 pairwise correlations are not as well reproduced, showing 455
 455 lower covariance in the generated data (Fig.4f). This 456
 456 mismatch presumably comes from the fact that the 457
 457 activities of neurons within a state are uncorrelated in 458
 458 our emission probabilities, while recurrent interactions 459
 459 in the ARTR circuit produce correlations. These would 460
 460 be better modeled with emission probabilities including 461
 461 effective interactions between neurons [27]. 462

463 F. Comparison of Behavior and Neuronal HMMs

464 In the preceding sections, we demonstrated that both
 465 the reorientation behavior and the neuronal activity of
 466 the *Anterior Rhombencephalic Turning Region* (ARTR)
 467 can be effectively modeled using three-state Hidden
 468 Markov Models (HMMs). However, it remains unclear
 469 whether the three states identified in the Behavioral
 470 HMM (B-HMM) directly correspond to those inferred in
 471 the Neuronal HMM (N-HMM).

472 Unfortunately, there is currently no publicly avail-
 473 able dataset offering simultaneous recordings of freely
 474 swimming larvae kinematics and neuronal activity, which
 475 would enable direct comparison of B-HMM and N-HMM
 476 states for individual bouts. Current research addressing
 477 this question largely relies on experimental paradigms
 478 where larvae are either paralyzed with electrophysiological
 479 recording of motor nerve signals (fictive swimming
 480 preparations)[18, 30, 31], or head-embedded with a free-
 481 moving tail (head tethered preparations)[32–35]. In fic-
 482 tively swimming preparations, whilst the classification
 483 of left-vs-right bouts is feasible based on the asymmet-
 484 ric nature of the motor command, such experiments lack
 485 the level of precision required to discriminate forward-
 486 vs-turning bouts [18]. On the other hand, head tethered
 487 preparations allow forward-left-right bout classification
 488 [32, 34], but typically rely on visual stimuli to elicit be-
 489 havior [32–35] as the spontaneous sequence of bouts is
 490 strongly disrupted in comparison with freely swimming
 491 contexts [36].

492 We hereafter propose to circumvent these experimental
 493 challenges by comparing the statistical structures of the
 494 reorientation sequences inferred from the two datasets
 495 presented in sections II A and II E. The transition prob-
 496 abilities $P(s_n \rightarrow s_{n+1})$ obtained from B-HMM and N-
 497 HMM at all recorded temperatures are shown in Fig.5b.
 498 Comparison of these transition rates require to first cor-
 499 rect them for differences in sampling rates. Indeed, neu-
 500 ral transition rates are computed from neuronal record-
 501 ings performed at ~ 6 Hz (depending on the dataset, see
 502 Materials and Methods IV B), while for behavior, the se-
 503 quences are divided into swim bouts triggered at an av-
 504 erage rate of ~ 1 Hz, depending on the temperature.

505 To bridge the gap between neuronal and behavioral
 506 datasets, one needs to estimate how the behavior is sub-
 507 sampled from the neuronal activity. To do so, we com-
 508 puted the distribution of sojourn times Δt_s of all three
 509 states in both B-HMM and N-HMM, where $\Delta t_s = t_k - t_1$
 510 is the duration of a sequence (s_1, \dots, s_k) of k consecutive
 511 states s observed at times (t_1, \dots, t_k) . We found the neu-
 512 ronal sojourn times to be significantly longer than the
 513 behavioral sojourn times (Fig.5a). The optimal tempo-
 514 ral scaling factor $f_{N/B}$ for which the distribution of neu-
 515 ronal sojourn times matches the distribution of behav-
 516 ioral sojourn times (see Materials and Methods IV G)
 517 was $f_{N/B} \approx 0.44$. Interestingly, this value appears to be
 518 consistent with findings from Dunn *et al.* [18], which re-
 519 ported the mean interbout interval for fictive swimming

520 to be 0.41 times slower than for freely swimming.

521 Using this temporal re-scaling factor, we find that the
 522 transition probabilities $P(s_n \rightarrow s_{n+1})$ for behavior and
 523 ARTR models are similar (RMSE = 0.1, see Fig.5b), in-
 524 dicating that the behavioral and neuronal state sequences
 525 share similar underlying structures. This is remarkable as
 526 the number and meaning of the neuronal internal states
 527 were not *a priori* fixed, but entirely assigned by N-HMM
 528 after training.

529 This result supports our hypothesis that the ARTR
 530 not only governs the selection between rightward and
 531 leftward turning bouts, but also controls the bout-type
 532 selection, forward *vs* turn. To test this claim further, we
 533 analyzed in more detail the statistics of trajectories in
 534 the bout space inferred from the ARTR dynamics and
 535 from behavioral data. We specifically examined the bout
 536 sequences leading to a change in orientation, such as
 537 transitions from L to R and vice-versa. Such orienta-
 538 tional switches can be either direct, e.g. $L \rightarrow R$, or
 539 may include an intermediate forward bout, $L \rightarrow F \rightarrow R$
 540 (Fig.5c). Using the ARTR signal, we found that the sec-
 541 ond path is strongly favored as evidenced by the the fact
 542 that $\frac{P(L \rightarrow R)}{P(L \rightarrow F)} \ll 1$. A comparable value of this ratio is
 543 observed in the behavioral data (Fig.5d), indicating that
 544 fish indeed tend to execute a forward bout when chang-
 545 ing orientation. This statistical bias would be difficult to
 546 understand under the standard model that posit the ex-
 547 istence of independent neural circuits governing orienta-
 548 tion and bout-type selection, respectively. In contrast, in
 549 our model, it emerges naturally from the the phase space
 550 structure of the ARTR dynamics as shown in Figure 4c
 551 and Figure 5c. The L-Shaped distribution of $\{m_L, m_R\}$
 552 constrains the Left-to-right (or Right-to-Left) trajecto-
 553 ries to pass through a symmetrical, low activity state,
 554 thus favoring intermediate forward bouts.

555 G. Generation of synthetic behavior with the 556 neural model

557 Until now, we compared neuronal and behavioral data
 558 by examining only the short-scale statistical structures
 559 of the HMM-inferred state sequences. We now wish to
 560 test whether it is possible to compare full trajectories
 561 by leveraging the generative nature of the HMM. Specif-
 562 ically, we use the N-HMM model to generate long syn-
 563 thetic trajectories and compare their statistics with those
 564 of freely swimming fish. This approach allows us to as-
 565 sess whether the N-HMM, when combined with appro-
 566 priate scaling and behavioral parameters, can reproduce
 567 the complex statistical properties of exploration at vari-
 568 ous temperatures.

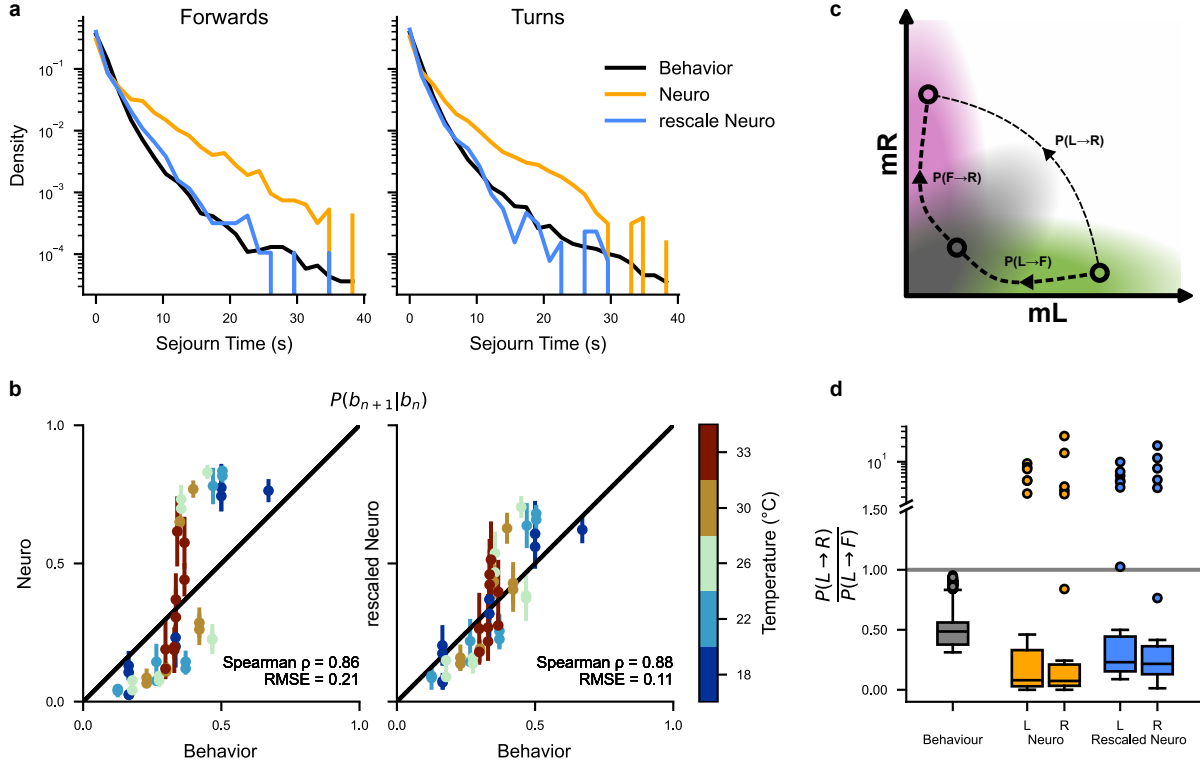


FIG. 5. **Behavior vs. Neuronal temporal structure:** (a) Distribution of forward and turn sojourn times for the behavior (black) and neuronal data before (orange) and after temporal re-scaling (magenta). A single re-scaling factor is used for forward and turning states, for all temperatures, and for all recordings. (b) Comparison of behavior and neuronal state-transition probabilities $P(s_n \rightarrow s_{n+1})$, before (left plot) and after (right plot) temporal re-scaling. Each dot represents a single transition probability at a given temperature. For neuronal state-transition, the mean and standard error of the mean for all recordings at specific temperatures are shown. (c) Diagram showing two possible transition trajectories between left and right states in ARTR mean-activity space. Transitions through the forward state are more probable (see panel d). (d) Distributions of $\frac{P(L \rightarrow R)}{P(L \rightarrow F)}$ the behavior (black) and neuronal data before (orange) and after temporal re-scaling (magenta), with all temperatures combined. These distributions are depicted as standard box plots (median and quartiles), as well as outlier points lying further than $1.5 \times$ the inter-quartile range from the median.

569 1. *Generation of synthetic neural and reorientation*
570 *trajectories*

571 As stochastic processes, Hidden Markov Models
572 (HMMs) can be sampled to generate new sequences of
573 internal states. Following the previous section IIF, we
574 hypothesize that the internal states of a Neural HMM (N-
575 HMM) match the behavioral internal states, after proper
576 temporal rescaling. Therefore, we expect that it should
577 be possible to generate artificial swim trajectories from
578 the N-HMMs.

579 Using the N-HMMs associated to individual fish
580 recordings, we started by generating synthetic temporal
581 sequences of neural states $s_n^N \in \{F, L, R\}$. We then sam-
582 pled the behavioral distribution of inter-bout intervals
583 δt_n , rescaled by the scaling factor $f_{N/B} \approx 0.44$ obtained
584 in the previous section IIF. This simulates a stochastic
585 bout-initiation process with the correct temporal char-
586 acteristics, yielding synthetic sequences of bout internal
587 states b_n for the behavior. For each state, we then sam-

588 ple the emission probability $E(\delta\theta_n|b_n)$ associated to the
589 Behavioral HMM (B-HMM) inferred from all fish data to
590 get a realization of the reorientation angle $\delta\theta_n$ (Fig. 6d).
591 As expected, the distribution of these angles is in very
592 good agreement with the ones observed in the behavioral
593 data (Fig. 6a).

594 We further characterize the trajectories using the Mean
595 Square Reorientation (MSR) after q bouts:

$$\text{MSR}(q) = \left\langle \left(\sum_{n=t+1}^{t+q} \delta\theta_n \right)^2 \right\rangle_t \quad (5)$$

596 where the average is taken across all times and all tra-
597 jectories.

598 Figure 6b shows the values of M_q obtained from N-
599 HMM-generated trajectories at different temperatures
600 (see Fig.S7 for the remaining temperatures), as well as
601 the MSR directly obtained from multiple-fish trajectories
602 and long single-fish trajectories (only at 26°C).

603 We first notice that long individual fish trajectories at
604 26°C display large variability in MSR(q) values, compati-

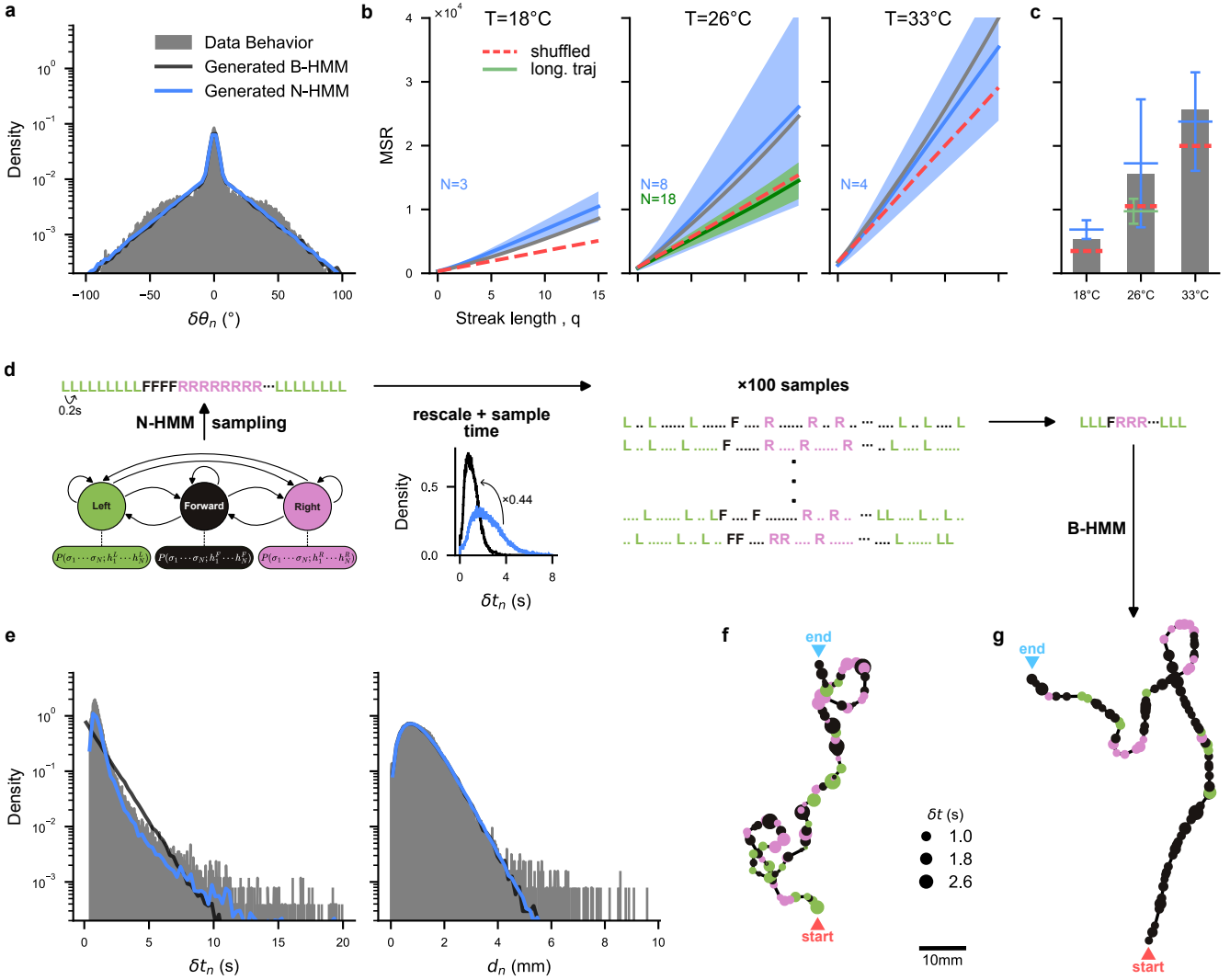


FIG. 6. Generative ability of HMM models and trajectory reconstruction: (a) Distribution of bout angles $\delta\theta_n$ for the aggregated multiple-fish trajectories (gray), generated trajectories from Behavioral Hidden Markov Models (B-HMM ; black), and generated trajectories from Neuronal Hidden Markov Models (N-HMM ; blue), at 22°C. (b) Mean Square Reorientation (MSR) accumulated after q bouts for aggregated multiple-fish trajectories (grey), shuffled aggregated multiple-fish trajectories (red dashed), single-fish long trajectories (green), and trajectories generated from N-HMM (blue). For both long and N-HMM-generated trajectories, the mean and standard deviation over all individual fish are shown (respectively with a solid line and filled band). (see Fig.S7 for individual trajectories and all temperatures) (c) Bar plot for the MSR at $q = 10$ bouts, with mean (horizontal bars) and standard deviation (vertical bars). (d) Diagram explaining the conversion from N-HMM generated state sequences to swim trajectories. The N-HMM is first sampled to generate a sequence of forward, left, right internal states. Time is then re-scaled using the scaling factor identified in Fig 5, and bout sequences are sampled 100 times based on the interbout interval distribution. A swim trajectory is constructed for each bout sequence by sampling the bout distances d_n and inter-bout intervals δt_n emission distributions in the B-HMM. (e) Distribution of inter-bout intervals δt_n and bout distances d_n for the aggregated multiple-fish trajectories (gray), generated trajectories from B-HMM (black), and generated trajectories from N-HMM (blue), at 22°C. (f) Example trajectory generated from B-HMM at 26°C. Point color corresponds to bout type (left, right, forward), and point size corresponds to inter-bout interval. (g) Same as panel f for a N-HMM-generated trajectory at 26°C.

605 ble with the presence of fish-to-fish variability. This vari-
 606 ability is washed out for the multiple-fish dataset (since
 607 individual trajectories are combined) providing a aver-
 608 aged MSR(q) for each temperature. Interestingly, the
 609 MSR for the long sequences of individual animals signif-

610 icantly differ from the MSR obtained from multiple-fish
 611 trajectories. This could be due to differences in experi-
 612 mental conditions, and in particular the effects of collec-
 613 tive vs. isolated navigation [22].

614 N-HMM-generated trajectories have a MSR distribu-

tion compatible and encompassing the behavioral data in their variability. Such large variability is expected from the large fluctuations in neural brain states. Some trajectories generated with N-HMM show anomalously large angular persistence (see Fig.S7a), which may correspond to brain states where the *Anterior Rhombencephalic Turning Region* (ARTR) displays no left-right alternating behavior. This is expected, as the N-HMMs were established from spontaneous activity recordings of immobilized fish which were not constrained to swim-like behaviors. In Fig. 6c, we summarized and compared the results for the Mean Square Reorientation after 10 bouts, $MSR(q = 10)$, for all temperatures. We found, consistently across temperatures, that the MSR of behavioral data are comprised within the one-standard-deviation confidence interval of N-HMM-generated trajectories.

As we show in the Appendix 1, the MSR of HMM-generated trajectories can be decomposed as the sum of a purely diffusive contribution, associated to the variance of bout angles, and of terms arising from time-correlations in bout type selection along a trajectory (see Eq. (A.28)). The increase of bout-angle variance with temperature is sufficient to explain the increasing trend of the mean MSR with temperature observed in Figure 6c (see Fig.S7).

2. Generation of synthetic 2D trajectories

For the sake of completeness, we also used the N-HMM model to generate full synthetic 2D trajectories. To do so, for each bout state identified with the procedure reported above, we sampled an inter-bout interval duration δt_n and traveled distance d_n from their experimental distributions. We then reconstructed the coordinates of the virtual fish after k bouts, (x_k, y_k) , through

$$x_k = \sum_{n=1}^k d_n \cos(\theta_n), \quad y_k = \sum_{n=1}^k d_n \sin(\theta_n), \quad (6)$$

where $\theta_n = \sum_{i=1}^n \delta\theta_i$ is the orientation angle of the fish at bout i , constructed as the cumulative sum of re-orientation angles at previous bouts. An example trajectory is shown in Fig. 6g, and is qualitatively similar to the experimental counterpart recorded at the same temperature.

For comparison, we show synthetic trajectories generated from behavioral HMM. In practice, we expanded on the B-HMM introduced in section IIB 2 by adding two new emission distributions corresponding to δt_n and d_n . As done previously, the HMMs were first trained only on the re-orientation angles $\delta\theta_n$, before learning the emission distributions for δt_n and d_n . We then plot the corresponding trajectories using Eq. (6), which are qualitatively similar to the N-HMM-generated ones, as illustrated by an example in Fig.6f. The similarity is quantified by the comparison of the distributions of bout angles,

inter-bout duration intervals and traveled distances, see Fig.6f.

We report in Figure S7e-h, the outcome of an intermediate generative model, in which 2D swim trajectories are generated from experimental neural recordings. This is done by first identifying neural states from the recordings using the Viterbi algorithm, emitting inter-bout intervals using the same procedure as described above, and then feeding the resulting state sequences through the B-HMM.

III. DISCUSSION

With the advancement of video-tracking and brain recording methods, behavioral neuroscience has changed radically in the last decade. It is now possible to study in great details animal behavior in unconstrained naturalistic conditions [37–39], while new recording methods give access to extended circuit activity encompassing several brain regions. Such experiments produce vast amounts of high-dimensional data, requiring automated yet robust and interpretable analysis methods.

An essential task is the identification of behavioral or neural states from the segmentation of the recorded time series, in order to extract low-dimensional representations that are easier to interpret. However, no definitive procedure exists for selecting the optimal number of states or for defining valid labeling criteria. This choice typically depends on available observables and involves a compromise between interpretability and accuracy of representation.

In our case, the difficulty stems from three main factors: (i) the dependence of swim bout kinematics with bath temperature, (ii) the inter-individual variability, and (iii) the overlapping distributions of reorientation angles for distinct bout types, in particular at low temperatures. Because they can accommodate such overlaps while taking into account the temporal regularities in the bout sequences, Hidden Markov Models (HMMs) are ideally suited for such a task. They are easily interpretable as the dynamics between the different internal states is described by a Markovian process. This makes HMM a powerful alternative to deep-learning-based methods, whose predictive power comes at the cost of interpretability.

In this study, we successfully applied a three-state HMM to parse behavioral and neural time series associated with exploratory dynamics. We showed that for behavioral data, HMM provided a less biased and more consistent method for bout-type labeling compared to standard threshold-based Markov Chain (MC) methods used in earlier studies.

This robustness proved essential as we investigated the effect of bath temperature on navigation. Zebrafish being cold-blooded animals, the water temperature is expected to directly affect muscle efficiency, leading to

720 a systematic increase in the amplitude of reorientation
 721 elicited by bouts as temperature rises. When using
 722 hard-threshold-based MC methods, this may lead to
 723 a systematic but artifactual increase in the fraction of
 724 bouts labeled as turns with temperature. With HMM,
 725 this physiological effect of temperature is naturally
 726 accounted for through an adaptive adjustment of the ef-
 727 fective threshold angle between turn and forward bouts.
 728 With this unbiased labeling, we found that the fractions
 729 of forward and turn bouts were only weakly dependent
 730 on temperature, in contrast with previously published
 731 analysis [22]. The primary effect of temperature of
 732 rising temperature is to progressively decrease bout-type
 733 persistence, i.e. the tendency of the animal to chain
 734 similar bouts. Interestingly, we found that all three bout
 735 types, and not just turns as previously reported, exhibit
 736 comparable persistence.

737

738 HMMs also demonstrated remarkable sensitivity to
 739 individual phenotypic variability. Inter- and intra-
 740 individual variability are ubiquitous traits of animal be-
 741 havior [40, 41] and are necessary to ensure a trade-off
 742 between flexibility and adaptability to changing environ-
 743 mental demands and robustness in neural development
 744 [42, 43]. In Le Goc *et al.* [22], inter-individual differences
 745 were demonstrated on the same dataset using multiple
 746 kinematic parameters (including inter-bout interval, for-
 747 ward travel distance or reorientation amplitude). In con-
 748 trast, our study shows that HMM can identify individual
 749 fish solely based on the dynamics of bout-type sequences.
 750 Moreover, HMM provides explicit likelihood evaluation
 751 for bout sequences for various individual-specific models,
 752 providing a quantitative measure of phenotypic proxim-
 753 ity between animals or across time.

754 Since our approach is based on gait phenotyping and
 755 is independent of image features, it is compatible with
 756 low-resolution videos (in which only the animal’s posi-
 757 tion and orientation can be accessed) while still keep-
 758 ing versatility, reliability, and fast execution. This opens
 759 new opportunities for studying phenotypic variation in
 760 swimming behavior, potentially uncovering subtle effects
 761 on behavior of genetic, developmental, or environmental
 762 cues. This ability to precisely capture behavioral vari-
 763 ability might also prove fruitful in order to explore the
 764 neural basis of individuality.

765 The fact that the fish directional dynamics can be
 766 described by a three-state Markovian sequence, suggests
 767 that bout-type selection is likely governed by a single
 768 circuit, with the ARTR being the most plausible can-
 769 didate. Since its discovery in 2012 [30], the ARTR has
 770 been viewed as a direction-selection hub, controlling lat-
 771 eralized behaviors such as tail flick and ocular saccade
 772 orientation [18, 44]. It also responds to lateralized vi-
 773 sual stimuli, including binocular contrast and whole-field
 774 lateral motion [20, 44].

775 In the present study, we showed that a three states
 776 HMM can accurately describe ARTR neuronal data, and
 777 that this model is structurally and temporally similar to

778 behaviorally-trained HMMs. This result suggests that
 779 the ARTR may also govern forward bout selection, uni-
 780 fying the control of all directional bout types within a
 781 single circuit. This interpretation is reinforced by the
 782 generation of synthetic, neuronally driven swimming se-
 783 quences that closely matched the statistics of observed
 784 trajectories.

785 Bout-type persistence, as observed in behavioral as-
 786 says, is mirrored in the slow sequential exploration of
 787 the three hidden states identified in neural recordings of
 788 the ARTR. Although the HMM enables the identifica-
 789 tion of these neuronal states, they provide no interpre-
 790 tation of how they emerge from interactions among the
 791 ARTR neuronal population. In fact, our implementation
 792 of HMM assumes the activity of neurons to be indepen-
 793 dent of each other when conditioned to a state.

794 In a recent study, we trained data-driven graphical
 795 models (Ising model) on ARTR activity sequences [27].
 796 The Ising model uses activity patterns to learn the inter-
 797 actions between neurons but, unlike HMM, it ignores any
 798 temporal information in the data. Interestingly, the in-
 799 ferred Ising models tended to display three metastable
 800 states, two with high activity on either side and one
 801 “equilibrated” state with intermediate, balanced activ-
 802 ity on both sides, consistent with the three hidden states
 803 found with HMM. This convergence underlines the com-
 804plementary strengths of state-space and energy-based
 805 models in elucidating neural dynamics. While the former
 806 might enable capturing the temporal structure in
 807 collective neural activity, the latter offer insights into the
 808 underlying network interactions driving these states, and
 809 how metastability emerges within neural populations.

810 The exact mechanism through which the ARTR con-
 811 trols bout selection remains unclear. However, our find-
 812 ings suggest that ARTR subpopulations (right and left)
 813 might inhibit contraversive bouts (*i.e.* when the left side
 814 is active, it suppresses rightward turns, favoring leftward
 815 swim). In the equilibrated state, both inhibitory sig-
 816 nals suppress turn bouts, leaving forward movement as
 817 the only option. Such a motor suppression mechanism is
 818 consistent with observations by Dunn *et al.* [18], which
 819 showed a continuous relationship between the lateral dif-
 820 ference in the ARTR activity and the mean reorientation
 821 angle of the executed bout. While our model strongly
 822 supports this hypothesis, definitive experimental valida-
 823 tion is required.

824 Last of all, to facilitate the accessibility and adoption
 825 of Hidden Markov Model (HMM) formalism for analyz-
 826 ing behavioral sequences, we provide a comprehensive
 827 and instructive Python tutorial (<https://github.com/EmeEmu/IBIO-Banyuls2023-Python>). This tutorial can
 828 be adapted for specific datasets or used as a resource for
 829 broader educational goals.

IV. MATERIALS AND METHODS

A. Behavioral Datasets

The behavioral dataset used in the present study is derived from Le Goc *et al.* [22], and can be accessed directly at <https://doi.org/10.5061/dryad.3r2280ggw>. This dataset comprises spontaneous swimming trajectories of 5 to 7 dpf zebrafish larvae, collected at controlled bath temperatures of 18°C, 22°C, 26°C, 30°C, and 33°C. A camera was used to continuously record the swimming behavior of the fish within an arena of 100×45×4.5mm³ for 30 minutes at 25 frames/second. To eliminate border effects, a Region of Interest (ROI) was defined at a distance of 5mm from the arena’s walls. Fish that swam outside the defined tracking ROI were considered lost, and a new trajectory was initiated upon their re-entry into the ROI. The identity of the fish is thus lost each time it exits the ROI. Therefore, the dataset contains a varying number of fish trajectories, ranging from 532 to 1513 trajectories across the different temperatures (mean = 1148). Individual trajectories were tracked offline using the open-source FastTrack software [45], and were then discretized into sequences of swimming bouts. Each trajectory consists of a sequence of swim bouts, spanning from 9 to 748 bouts per trajectory (mean=60, distributions shown in Fig.S1a). From this extensive dataset, we primarily utilized the re-orientation angles, defined as the difference between the heading direction at bout $n + 1$ and the heading direction at bout n :

$$\delta\theta_n = \theta_{n+1} - \theta_n \quad (7)$$

(a graphical illustration of this definition can be found in Fig.1c). This parameter encapsulates the angular change between consecutive bouts, providing insight into the fish’s ability to modify its orientation during swimming.

We also used the interbout interval $\delta t_n = t_{n+1} - t_n$ representing the elapsed time between 2 consecutive bouts, and the traveled distance $d_n = \|\vec{r}_{n+1} - \vec{r}_n\|$.

On top of these multi-fish trajectories, we used in sections IID and IIG a second dataset from Le Goc *et al.* [22] consisting in single-fish recordings. For this dataset, each fish (N=18) is placed alone in the arena at 26°C, and is recorded for 2 hours. With this experimental paradigm, the identity of the fish is conserved across trajectories, even when the fish leaves and re-enters the ROI.

B. Neuronal Datasets

The neuronal dataset used in the present study is derived from Wolf *et al.* [27], and can be accessed directly at https://gin.g-node.org/Debregeas/ZF_ARTR_thermo. This dataset contains 32 one-photon Light-Sheet Microscopy recordings of spontaneous brain activity, for 13 zebrafish larvae (5 to 7 dpf) at 18°C,

22°C, 26°C, 30°C, and 33°C. It focuses on neurons from the *Anterior Rhombencephalic Turning Region* (ARTR), with ~ 300 neurons (mean 307, std 119), recorded during ~ 20 min (mean 23, std 4 min) at ~ 6 Hz (mean 5.9, std 2.1 Hz).

C. Emission of reorientation angles in the Hidden Markov Model

To validate the hypothesis that the re-orientation angles can be modeled using normal and gamma distributions, we compared the distribution of the data with a Gaussian Mixture Model (GMM) and a Gaussian&Gamma Mixture Model:

$$p(\delta\theta) = w_F \mathcal{N}(\delta\theta; 0, \sigma) + w_L \Gamma(\delta\theta; \alpha, \theta) + w_R \Gamma(-\delta\theta; \alpha, \theta)$$

where $w_F + w_L + w_R = 1$, and w_F , w_L , and w_R denote the weights for forward, left, and right states, respectively.

Using Quantile-Quantile (QQ) plots, we show that this last mixture model accurately reproduces the observed distribution of $\delta\theta_n$ in the data, and is much better than a GMM, especially in the tails of the distributions (Fig. S2a). We also confirmed that, once trained, the emission distributions do indeed match the observed reorientation distributions (Fig. S2b-c).

D. Stubbornness factor

The *stubbornness* factor f_q is a measurement of the animal’s preference towards turning in the same direction over changing direction, after q intermediary forward bouts (Fig.S4c), as defined in (3).

It can be computed from a sequence of classified bouts b_n by first identifying and counting the q -plets $T_1 \rightarrow F^q \rightarrow T_2$ where $T_1 = T_2$ and where $T_1 \neq T_2$:

$$\begin{cases} N_{=} & = \#(T_1 \rightarrow F^q \rightarrow T_2, T_1 = T_2) \\ N_{\neq} & = \#(T_1 \rightarrow F^q \rightarrow T_2, T_1 \neq T_2) \end{cases} \quad (8)$$

and then computing their ratio:

$$f_q = \frac{N_{=}}{N_{\neq}} \quad (9)$$

In practice, this ratio has a physical interpretation only for long sequences of bouts where $N_{=} \gg 1$ and $N_{\neq} \gg 1$. As the trajectories in our dataset can be quite short (Fig. S1a), we compute f_q from all trajectories at a specific temperature, increasing the chance of observing a high number of stubborn ($N_{=}$) and non-stubborn (N_{\neq}) trajectories.

By considering that the probability of a given q -plet is stubborn follows a binomial distribution ($\mathbb{E}(N_{=}) = pN$

921 and $\mathbb{E}(N_{\neq}) = (1 - p)N$ with $N = N_{=} + N_{\neq}$, we can
 922 evaluate the uncertainty in *stubbornness* as:

$$\Delta f_q = f_q \frac{1}{N_{=} + N_{\neq}} \left(\sqrt{\frac{N_{=}}{N_{\neq}}} + \sqrt{\frac{N_{\neq}}{N_{=}}} \right) \quad (10)$$

923 It is to be noted that these uncertainties are conser-
 924 vative estimates, as there exists a bias inherent to the
 925 dataset. Indeed, a very stubborn fish will tend to stay
 926 longer within the Region Of Interest (ROI) of the cam-
 927 era, leading to longer trajectories and therefore weighing
 928 more on the final result. Hence, it is unclear whether a
 929 *stubbornness* factor $f_q = 1 \pm 0.2$ is truly significant (as
 930 suggested by the estimated error bars on Fig.S4d).

931 Furthermore, as the stubbornness factor is computed
 932 from all trajectories (and thus all fish) at a particular
 933 temperature, it represents an average behavior rather
 934 than an individual fish.

935

936 E. Stubbornness factor and 3-state Markov Chain

937 The *stubbornness* factor can be defined directly from
 938 the transition matrix.

939 For $q = 0$, calculations are simple:

$$f_{q=0} = \frac{P(L \rightarrow L) + P(R \rightarrow R)}{P(L \rightarrow R) + P(R \rightarrow L)} \quad (11)$$

940 For $q \geq 1$, the *stubbornness* factor is defined from
 941 the transition matrix as:

$$\begin{aligned} S_{L,q} &= P(L \rightarrow F^q \rightarrow L) \\ &= P(L)P(L \rightarrow F)P^q(F \rightarrow F)P(F \rightarrow L) \\ W_{L,q} &= P(L \rightarrow F^q \rightarrow R) \\ &= P(L)P(L \rightarrow F)P^q(F \rightarrow F)P(F \rightarrow R) \\ f_q &= \frac{S_{L,q} + S_{R,q}}{W_{L,q} + W_{R,q}} \end{aligned}$$

942 with $S_{L,q}$ the probability of a trajectory which starts and
 943 ends with a left bout, $W_{L,q}$ the probability of a trajectory
 944 which starts with a left bout and ends with a right bout,
 945 and $S_{R,q}$ $W_{R,q}$ their symmetrical opposites.

946 For a 3-state model, the forward-forward bout proba-
 947 bility cancels out, giving:

$$f_q = \frac{P(L)P(L \rightarrow F)P(F \rightarrow L) + P(R)P(R \rightarrow F)P(F \rightarrow R)}{P(L)P(L \rightarrow F)P(F \rightarrow R) + P(R)P(R \rightarrow F)P(F \rightarrow L)}$$

948 and with our non-handedness hypothesis: $P(L) = P(R)$,
 949 $P(L \rightarrow F) = P(R \rightarrow F)$, and $P(F \rightarrow L) = P(F \rightarrow R)$,
 950 yielding:

$$f_q = 1 \quad \forall q > 0 \quad (12)$$

952 F. Labeling of states in the neuronal Hidden Markov Model

953 The internal states of the Hidden Markov Models
 954 (HMMs) trained from neuronal activity are not *a pri-*
 955 *ory* assigned to the Left, Right and Forward labels, and
 956 must therefore be re-ordered post-training.

957 We expect a certain symmetry in the system, where
 958 neurons in the left side of the ARTR will be more active
 959 during a Left state (and vice versa). Hence, we can use
 960 the excitability h_i^s of neuron i in each internal state s ,
 961 as defined in the emission distribution of the HMM (see
 962 Eq. 4). We define the lateralized excitability:

$$\Delta h^s = \langle l(h_i^s) \rangle_{i \in \mathcal{L}} - \langle l(h_i^s) \rangle_{i \in \mathcal{R}} \quad (13)$$

963 where $l(x) = \frac{1}{1+e^{-x}}$ is the standard logistic function, and
 964 \mathcal{L} and \mathcal{R} are the sets of neurons located respectively in
 965 the left and right side of the ARTR. We thus label the
 966 HMM states such that

$$\Delta h^L > \Delta h^F > \Delta h^R \quad (14)$$

967 with F , L , and R the Forward, Left and Right internal
 968 states.

969

G. Temporal re-scaling

970 To find the temporal re-scaling factor $f_{N/B}$ between
 971 behavioral and neuronal models, we first compute the dis-
 972 tributions of sojourn times Δt_s for all states $s \in \{F, L, R\}$
 973 in both behavioral and neuronal Hidden Markov Models.

974 We then find the optimal re-scaling factor $f_{N/B}$ for
 975 which the combined distributions $\Delta t_b = [\Delta t_F^b, \Delta t_L^b, \Delta t_R^b]$
 976 and $\Delta t_n = [\Delta t_F^n, \Delta t_L^n, \Delta t_R^n]$ are as close to each other as
 977 possible :

$$f_{N/B} = \min_{f \in [0,1]} \text{RMSE}(Q(\Delta t_b), f \cdot Q(\Delta t_n)) \quad (15)$$

978 where $Q(D)$ is the quantiles of a distribution D , and
 979 $\text{RMSE}(\mathbf{x}, \mathbf{y})$ is the Root Mean Squared Error between
 980 vectors \mathbf{x} and \mathbf{y} (see Fig.S6a).

981

982 For Markov chains, the transition matrix $P = P(s_n =$
 983 $s \rightarrow s_{n+1} = s')$ represents the probability of transitioning
 984 in one step from state s to state s' . The transition proba-
 985 bility $s \rightarrow s'$ in $k \in \mathbb{N}_1$ steps $P(s_n = s \rightarrow s_{n+k} = s')$ is
 986 then the matrix power P^k .

987 In order to apply the temporal re-scaling $f_{N/B}$ between
 988 behavioral and neuronal models, we can thus compute
 989 the re-scaled transition matrix :

$$P_n^* = P_n^{\lfloor \frac{\nu}{f_{N/B}} \rfloor} \quad (16)$$

990 where P_n is the transition matrix inferred from neuronal
 991 data recorded at a frequency ν Hz.

H. Mean Square Reorientation

992

1016

993 To characterize the orientational diffusivity of the tra-
994 jectories, we use the Mean Square Reorientation (MSR)
995 accumulated after q bouts, as defined in equation (5) [20].

996 For infinitely large datasets with no left-right bias,
997 we expect a centered distribution of reorientation angles
998 $\langle \delta\theta_n \rangle_n = 0$. However, this is not the case, particularly
999 for the neuronal dataset where experimental limitations
1000 can induce strong biases. In particular, two of those limi-
1001 tations are due to the one-sided illumination in our Light
1002 Sheet Fluorescence Microscope [46]. First, due to scat-
1003 tering, the illumination beam is not uniform left-right
1004 across the brain, which can induce biases in the detection
1005 of neurons and their activity. Second, the non-uniform
1006 perception of light by the zebrafish larvae can elicit a pho-
1007 totaxis response, which is known to bias the activity of
1008 the *Anterior Rhombencephalic Turning Region* (ARTR)
1009 [44].

1010 Since a non-zero bias can result in a distortion of
1011 the MSR (see Appendix 1), the MSR is computed from
1012 $\delta\hat{\theta}_n = \delta\theta_n - \langle \delta\theta_n \rangle_n$ instead of $\delta\theta_n$.

1013 **Acknowledgment.** We acknowledge the following fund-
1014 ing:

Author	Funder
M. DK.	École Doctorale Frontière de l'Innovation en Recherche et Education - Programme Bettencourt
J. FdCD.	Université PSL, AI Junior Fellow program
M. C.	European Union, Horizon 2020 Programme (H2020 MSCA ITN Project SmartNets GA-860949)
V. B.	European Research Council (ERC) under the European Union's Horizon 2020 research innovation program grant agreement number 715980
R. M., G. D., S. C.	Locomat ANR-21-CE16-0037

1015

1017 **Data and Code availability.** All the data
1018 and code used in the present article are avail-
1019 able under GNU General Public License version
1020 3 at <https://github.com/ZebrafishHMM2023/>
1021 [CodeAndData/tree/bioRxiv](https://github.com/ZebrafishHMM2023_CodeAndData/tree/bioRxiv).

1022 The custom Julia implementation of Hidden
1023 Markov Model used is available under MIT Li-
1024 cense at <https://github.com/ZebrafishHMM2023/>
1025 [ZebrafishHMM2023.jl/tree/bioRxiv](https://github.com/ZebrafishHMM2023.jl/tree/bioRxiv).

1026 We also provide two tutorials for the use of Hid-
1027 den Markov Models for behavioral sequence analysis.
1028 The first one was created for the Cogmaster "Ma-
1029 chine learning for cognitive science" course, and is
1030 available at [https://github.com/CoccoMonassonLab/](https://github.com/CoccoMonassonLab/ZebrafishHMM)
1031 [ZebrafishHMM](https://github.com/CoccoMonassonLab/ZebrafishHMM). The second one was created for the i-Bio
1032 Summer School "Advanced Computational Analysis for
1033 Behavioral and Neurophysiological Recordings" held in
1034 Banyuls-sur-Mer in the summer of 2023, and is available
1035 under GNU General Public License version 3 at [https://](https://github.com/EmeEmu/IBIO-Banyuls2023-Python)
1036 github.com/EmeEmu/IBIO-Banyuls2023-Python.

- 1037 [1] N. Tinbergen, *The study of instinct* (Pygmalion Press, 1051
1038 an imprint of Plunkett Lake Press, 2020). 1052
- 1039 [2] A. B. Wiltschko, M. J. Johnson, G. Iurilli, R. E. Peter- 1053
1040 son, J. M. Katon, S. L. Pashkovski, V. E. Abraira, R. P. 1054
1041 Adams, and S. R. Datta, Mapping sub-second structure 1055
1042 in mouse behavior, *Neuron* **88**, 1121 (2015). 1056
- 1043 [3] J. M. Mueller, P. Ravbar, J. H. Simpson, and J. M. Carl- 1057
1044 son, *Drosophila melanogaster* grooming possesses syn- 1058
1045 tax with distinct rules at different temporal scales, *PLoS* 1059
1046 *computational biology* **15**, e1007105 (2019). 1060
- 1047 [4] T. Gallagher, T. Bjorness, R. Greene, Y.-J. You, and 1061
1048 L. Avery, The geometry of locomotive behavioral states 1062
1049 in *c. elegans*, *PloS one* **8**, e59865 (2013). 1063
- 1050 [5] L. Tao, S. Ozarkar, J. M. Beck, and V. Bhandawat, Sta- 1064

tistical structure of locomotion and its modulation by odors, *Elife* **8**, e41235 (2019).

- [6] S. Linderman, A. Nichols, D. Blei, M. Zimmer, and L. Paninski, Hierarchical recurrent state space models reveal discrete and continuous dynamics of neural activity in *c. elegans*, *bioRxiv* 10.1101/621540 (2019).

- [7] G. J. Berman, W. Bialek, and J. W. Shaevitz, Predictability and hierarchy in *drosophila* behavior, *Proceedings of the National Academy of Sciences* **113**, 11943 (2016), <https://www.pnas.org/doi/pdf/10.1073/pnas.1607601113>.

- [8] R. E. Johnson, S. Linderman, T. Panier, C. L. Wee, E. Song, K. J. Herrera, A. Miller, and F. Engert, Probabilistic models of larval zebrafish behavior reveal struc-

- ture on many scales, *Current Biology* **30**, 70 (2020).
- [9] M. Breakspear, enDynamic models of large-scale brain activity, *Nat Neurosci* **20**, 340 (2017).
- [10] L. Mazzucato, A. Fontanini, and G. La Camera, Dynamics of multistable states during ongoing and evoked cortical activity, *Journal of Neuroscience* **35**, 8214 (2015), <https://www.jneurosci.org/content/35/21/8214.full.pdf>.
- [11] A. J. Quinn, D. Vidaurre, R. Abeysuriya, R. Becker, A. C. Nobre, and M. W. Woolrich, Task-evoked dynamic network analysis through hidden markov modeling, *Frontiers in neuroscience* **12**, 603 (2018).
- [12] Y. Zhang and S. Saxena, Inference of neural dynamics using switching recurrent neural networks, in *The Thirtieth Annual Conference on Neural Information Processing Systems* (2024).
- [13] M. B. Orger and G. G. de Polavieja, Zebrafish behavior: opportunities and challenges, *Annual review of neuroscience* **40**, 125 (2017).
- [14] J. R. Meyers, Zebrafish: development of a vertebrate model organism, *Current Protocols Essential Laboratory Techniques* **16**, e19 (2018).
- [15] J. H. Bollmann, The zebrafish visual system: from circuits to behavior, *Annual review of vision science* **5**, 269 (2019).
- [16] J. C. Marques, S. Lackner, R. Félix, and M. B. Orger, Structure of the zebrafish locomotor repertoire revealed with unsupervised behavioral clustering, *Current Biology* **28**, 181 (2018).
- [17] X. Chen and F. Engert, Navigational strategies underlying phototaxis in larval zebrafish, *Frontiers in Systems Neuroscience* **8**, 10.3389/fnsys.2014.00039 (2014).
- [18] T. W. Dunn, Y. Mu, S. Narayan, O. Randlett, E. A. Naumann, C.-T. Yang, A. F. Schier, J. Freeman, F. Engert, and M. B. Ahrens, Brain-wide mapping of neural activity controlling zebrafish exploratory locomotion, *Elife* **5**, e12741 (2016).
- [19] E. J. Horstick, Y. Bayleyen, J. L. Sinclair, and H. A. Burgess, Search strategy is regulated by somatostatin signaling and deep brain photoreceptors in zebrafish, *BMC biology* **15**, 1 (2017).
- [20] S. Karpenko, S. Wolf, J. Lafaye, G. Le Goc, T. Panier, V. Bormuth, R. Candelier, and G. Debrégeas, From behavior to circuit modeling of light-seeking navigation in zebrafish larvae, *eLife* **9**, e52882 (2020), publisher: eLife Sciences Publications, Ltd.
- [21] E. J. Horstick, Y. Bayleyen, and H. A. Burgess, Molecular and cellular determinants of motor asymmetry in zebrafish, *Nature Communications* **11**, 1170 (2020).
- [22] G. Le Goc, J. Lafaye, S. Karpenko, V. Bormuth, R. Candelier, and G. Debrégeas, Thermal modulation of Zebrafish exploratory statistics reveals constraints on individual behavioral variability, *BMC Biology* **19**, 208 (2021).
- [23] D. L. Barabási, G. F. Schuhknecht, and F. Engert, Functional neuronal circuits emerge in the absence of developmental activity, *Nature Communications* **15**, 364 (2024).
- [24] M. Haesemeyer, D. N. Robson, J. M. Li, A. F. Schier, and F. Engert, A brain-wide circuit model of heat-evoked swimming behavior in larval zebrafish, *Neuron* **98**, 817 (2018).
- [25] M. Haesemeyer, D. N. Robson, J. M. Li, A. F. Schier, and F. Engert, A brain-wide circuit model of heat-evoked swimming behavior in larval zebrafish, *Neuron* **98**, 817 (2018).
- [26] V. Palieri, E. Paoli, Y. Wu, M. Haesemeyer, I. Grunwald Kadow, and R. Portugues, The preoptic area and dorsal habenula jointly support homeostatic navigation in larval zebrafish, *Curr Biol* **3**, 34 (2024).
- [27] S. Wolf, G. Le Goc, G. Debrégeas, S. Cocco, and R. Monasson, Emergence of time persistence in a data-driven neural network model, *eLife* **12**, e79541 (2023).
- [28] J. Bezanson, A. Edelman, S. Karpinski, and V. B. Shah, Julia: A fresh approach to numerical computing, *SIAM review* **59**, 65 (2017).
- [29] G. Dalle, Hiddenmarkovmodels.jl: generic, fast and reliable state space modeling, *Journal of Open Source Software* **9**, 6436 (2024).
- [30] M. B. Ahrens, J. M. Li, M. B. Orger, D. N. Robson, A. F. Schier, F. Engert, and R. Portugues, Brain-wide neuronal dynamics during motor adaptation in zebrafish, **485**, 471 (2012), 22622571.
- [31] K.-H. Huang, M. B. Ahrens, T. W. Dunn, and F. Engert, Spinal Projection Neurons Control Turning Behaviors in Zebrafish, **23**, 1566 (2013).
- [32] L. Petrucco, H. Lavian, Y. K. Wu, F. Svara, V. Štih, and R. Portugues, Neural dynamics and architecture of the heading direction circuit in zebrafish, **26**, 765 (2023).
- [33] R. Portugues, C. E. Feierstein, F. Engert, and M. B. Orger, Whole-Brain Activity Maps Reveal Stereotyped, Distributed Networks for Visuomotor Behavior, **81**, 1328 (2014), 24656252.
- [34] E. I. Dragomir, V. Štih, and R. Portugues, Evidence accumulation during a sensorimotor decision task revealed by whole-brain imaging, **23**, 85 (2020).
- [35] K. E. Severi, R. Portugues, J. C. Marques, D. M. O'Malley, M. B. Orger, and F. Engert, Neural control and modulation of swimming speed in the larval zebrafish, **83**, 692 (2014), 25066084.
- [36] S. Karpenko, Naviguer avec la lumière : Du comportement aux circuits neuronaux chez la larve de poisson zèbre (2020).
- [37] A. E. Brown and B. De Bivort, Ethology as a physical science, *Nature Physics* **14**, 653 (2018).
- [38] T. D. Pereira, J. W. Shaevitz, and M. Murthy, Quantifying behavior to understand the brain, *Nature neuroscience* **23**, 1537 (2020).
- [39] A. Kennedy, The what, how, and why of naturalistic behavior, *Current opinion in neurobiology* **74**, 102549 (2022).
- [40] K. Honegger and B. de Bivort, Stochasticity, individuality and behavior, *Current Biology* **28**, R8 (2018).
- [41] A. K. Shaw, Causes and consequences of individual variation in animal movement, *Movement ecology* **8**, 12 (2020).
- [42] P. R. Hiesinger and B. A. Hassan, The evolution of variability and robustness in neural development, *Trends in Neurosciences* **41**, 577 (2018).
- [43] G. Sridhar, M. Vergassola, J. C. Marques, M. B. Orger, A. C. Costa, and C. Wyart, Uncovering multiscale structure in the variability of larval zebrafish navigation, *Proceedings of the National Academy of Sciences* **121**, e2410254121 (2024).
- [44] S. Wolf, A. M. Dubreuil, T. Bertoni, U. L. Böhm, V. Bormuth, R. Candelier, S. Karpenko, D. G. Hildebrand, I. H. Bianco, R. Monasson, *et al.*, Sensorimotor computation underlying phototaxis in zebrafish, *Nature communications* **8**, 651 (2017).
- [45] B. Gallois and R. Candelier, Fasttrack: an open-source

1193 software for tracking varying numbers of deformable objects, *PLoS computational biology* **17**, e1008697 (2021).
 1194
 1195 [46] T. Panier, S. Romano, R. Olive, T. Pietri, G. Sumbre, R. Candelier, and G. Debrégeas, Fast functional imaging of multiple brain regions in intact zebrafish larvae using Selective Plane Illumination Microscopy, *Frontiers in Neural Circuits* **7** (2013).
 1196
 1197
 1198
 1199

a. MSR for the HMM

1225 As an illustration, we can compute all these quantities exactly for the HMM as follows. For the autocorrelation, we have:
 1226
 1227

$$\begin{aligned}
 A_t &= \text{tr}_{h_0, \dots, h_t} P(h_t|h_{t-1}) \dots P(h_2|h_1) P(h_1|h_0) P(h_0) \\
 &\quad \times \left[\int P(\delta\theta|h_0) d\delta\theta \right] \left[\int P(\delta\theta|h_t) d\delta\theta \right] \\
 &= \text{tr}_{h, h'} [\Omega^t]_{h', h} P(h) \langle \delta\theta|h \rangle \langle \delta\theta|h' \rangle
 \end{aligned} \tag{A.22}$$

APPENDICES

1. Mean squared reorientation

1202 The mean-square reorientation (MSR) of a trajectory at lag q is defined as [20]:

$$M_q = \text{E} \left[\left(\sum_{i=1}^q \delta\theta_{t+i-1} \right)^2 \right] = \sum_{i,j=1}^q \text{E} [\delta\theta_{t+i-1} \delta\theta_{t+j-1}] \tag{A.17}$$

1204 where it is assumed that $\text{E}[\delta\theta] = 0$. The average is taken over time t . Assuming equilibrium, this is independent of t , and should depend only on the separation $|i-j|$,

$$\text{E} [\delta\theta_{t+i-1} \delta\theta_{t+j-1}] = \text{E} [\delta\theta_i \delta\theta_j] = A_{|i-j|} \tag{A.18}$$

1207 where $A_{|i-j|}$ stands for the time equilibrated autocorrelation function:

$$A_t = \lim_{t_0 \rightarrow \infty} \text{E} [\delta\theta_{t_0} \delta\theta_{t_0+t}] \tag{A.19}$$

1209 In particular $A_0 = \text{E}[\delta\theta^2]$ is just the variance of $\delta\theta$. It follows that,

$$\begin{aligned}
 M_q &= \sum_{i,j=1}^q A_{|i-j|} = \sum_{t=0}^{q-1} \left(\sum_{i,j=1}^q \delta_{|i-j|, t} \right) A_t \\
 &= qA_0 + 2 \sum_{t=1}^{q-1} \left(\sum_{i < j} \delta_{j-i, t} \right) A_t \\
 &= qA_0 + 2 \sum_{t=1}^{q-1} (q-t) A_t
 \end{aligned} \tag{A.20}$$

1211 Note that for a random walk without any correlations across time, $A_t = 0$ for $t > 0$. In this case, $M_q = qA_0$ grows linearly with q .

1214 On the other hand, it is expected that $A_t \rightarrow 0$ as $t \rightarrow \infty$, and usually this decay is exponentially fast in time. Therefore, for large q , we get the following asymptotic expression for M_q :

$$M_q \sim \left(A_0 + 2 \sum_{t=1}^{\infty} A_t \right) q - 2 \sum_{t=1}^{\infty} t A_t \tag{A.21}$$

1218 Notice that this is affine in q , with the coefficient $A_0 + 2 \sum_{t=1}^{\infty} A_t$. Therefore, M_q is initially linear in q with slope A_0 for small q , then has an elbow and eventually approaches the asymptotic slope $A_0 + 2 \sum_{t=1}^{\infty} A_t$ as $q \rightarrow \infty$. This asymptotic slope is different from A_0 only if the process exhibits non-trivial autocorrelations in time.

1228 where $[\Omega]_{h', h} = P(h'|h)$ is the transition matrix of the HMM. We will assume here that the initial state is sampled from $P(h) = p_{\text{eq}}(h)$, the equilibrium distribution of hidden states of the HMM, which satisfies the stationarity equation:

$$\text{tr}_h \Omega_{h', h} p_{\text{eq}}(h) = p_{\text{eq}}(h') \tag{A.23}$$

1233 Note also that $\text{E}[\delta\theta] = 0$ implies that $\sum_h p_{\text{eq}}(h) \langle \delta\theta|h \rangle = 0$. Now let $p_1(h), \dots, p_L(h)$ denote the remaining eigenvectors of Ω , with the associated eigenvalues $\lambda_1, \dots, \lambda_L$. By the Perron-Frobenius theorem, these remaining eigenvalues are all smaller than one in absolute value. The vector $P(h) \langle \delta\theta|h \rangle$ can be written in the basis of this eigenvectors,

$$P(h) \langle \delta\theta|h \rangle = \alpha_{\text{eq}} p_{\text{eq}}(h) + \sum_{i=1}^L \alpha_i p_i(h) \tag{A.24}$$

1240 for some coefficients $\alpha_{\text{eq}}, \alpha_1, \dots, \alpha_L$. Then it follows that,

$$\begin{aligned}
 A_t &= \text{tr}_{h'} \left[\alpha_{\text{eq}} p_{\text{eq}}(h') + \sum_i \lambda_i^t \alpha_i p_i(h') \right] \langle \delta\theta|h' \rangle \\
 &= \sum_i \alpha_i \lambda_i^t \text{tr}_{h'} p_i(h') \langle \delta\theta|h' \rangle
 \end{aligned} \tag{A.25}$$

1241 Since the $|\lambda_i| < 1$ it follows that $A_t \rightarrow 0$ exponentially fast as $t \rightarrow \infty$. Moreover we can compute,

$$\sum_{t=0}^{\infty} A_t = \sum_i \frac{\alpha_i}{1 - \lambda_i} T_i, \quad \sum_{t=0}^{\infty} t A_t = \sum_i \frac{\alpha_i \lambda_i}{(1 - \lambda_i)^2} T_i \tag{A.26}$$

1243 where

$$T_i = \text{tr}_h p_i(h) \langle \delta\theta|h \rangle \tag{A.27}$$

1244 These expressions then give a complete and exact characterization of the MSR for the HMM.
 1245

b. Standardized MSR

1247 The MSR as defined in Eq. A.17 includes both the diffusive contribution from the initial term A_0 and contributions arising from non-trivial time correlations in the

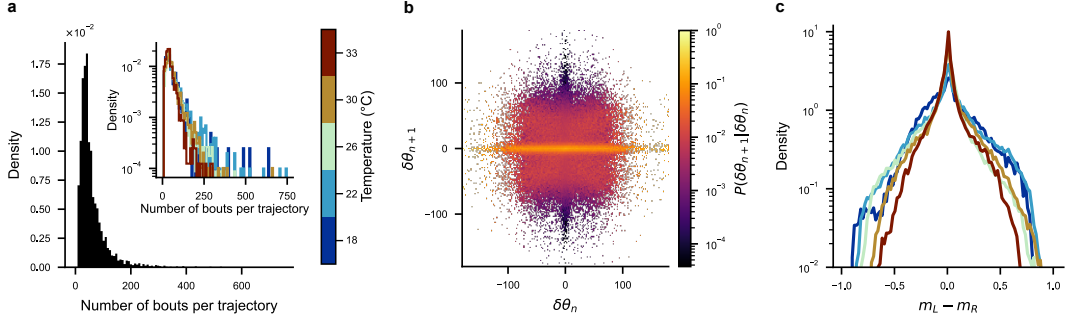


FIG. S1. **Supplementary panels to Fig. 1:** (a) Distributions of the number of bouts per trajectory in the entire behavioral dataset (black), and for each recorded temperature (inset, colored). (b) Observed transition probabilities between reorientation angles for the entire behavioral dataset. (c) Distributions of the difference between mean activities in the left (m_L) and right (m_R) *Anterior Rhombencephalic Turning Region* for all fish at each recorded temperature.

1250 process coming from the terms A_t for $t > 0$. As already 1258 large q .
 1251 pointed out, this initial term $A_0 = E[\delta\theta^2]$ is just the vari- 1259
 1252 ance of the distribution of bout angles and is insensitive 1260
 1253 to time correlations. To emphasize the time correlations 1261
 1254 we may normalize the trajectories by defining:

$$\hat{M}_q = \frac{M_q}{A_0} \quad (\text{A.28})$$

1255 By comparing with Eq. A.21, we see that \hat{M}_q has initially 1268
 1256 a slope ≈ 1 for small q , then has an elbow and eventually 1269
 1257 approaches the asymptotic slope $1 + 2 \sum_{t=1}^{\infty} A_t/A_0$ for 1270

1262 compare the time correlations of very diverse trajecto-
 1263 ries because it is insensitive to variations of $E[\delta\theta^2]$. Fig-
 1264 ure S7c-d plots the normalized MSR from Eq. (A.28) for
 1265 the various trajectories and temperatures considered be-
 1266 fore in Figure S7c-d. We observe that the standardized
 1267 MSR exhibits comparable behavior across various tem-
 1268 peratures, suggesting that the trend of the unnormalized
 1269 MSR observed in Figures 6b-c and S7a-b is just due to an
 1270 increase in the bout angle amplitudes $E[\delta\theta^2]$ with tem-
 perature, but not due to changes in the structure of their
 time correlations.

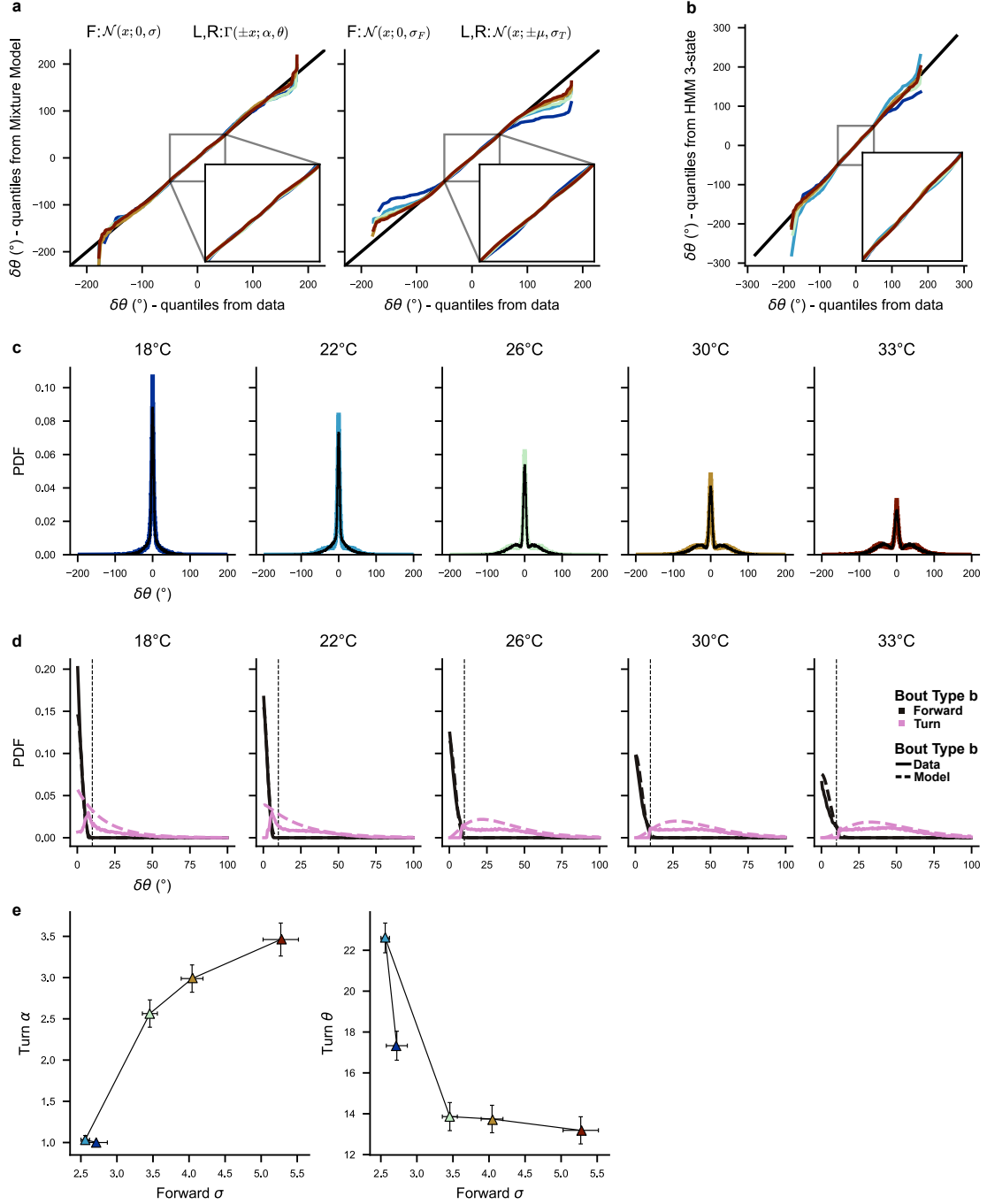


FIG. S2. **Supplementary panels to Fig. 2 - Emission distributions:** (a) Quantile-Quantile plot between distributions of reorientation angles observed from the data and Mixture Models, at each temperature. *Left:* Mixture Model defined from a central Normal distribution (forward bouts) and two Gamma distributions (left and right turning bouts), corresponding to the model of HMM emissions. *Right:* Gaussian Mixture Model. *Insets:* Zoom on $\pm 50^\circ$. (b) Quantile-Quantile plot between the distributions of reorientation angles observed from the data and the distributions of reorientation angles generated by HMM. *Insets:* Zoom on $\pm 50^\circ$. (c) Comparison between the distributions of reorientation angles observed from the data (colored) and the distributions of reorientation angles generated by the 3-state Hidden Markov Model (HMM; black), for each temperature. (d) Distributions of absolute reorientation angles labeled as forward bouts (solid black) and turning bouts (left or right; solid pink) by the Hidden Markov Model (HMM). Dashed lines show the HMM emission distribution for forward and turning bouts (black and pink respectively). The threshold $\delta\theta_0 = 10^\circ$ used in the Markov Chain model is shown for reference as a vertical black line. (e) Parameters of the HMM emission distribution, with σ the standard deviation of the central Normal distribution (forward bouts), α and θ the shape and scale of the Gamma distribution (turning bouts). Each dot corresponds to one temperature, and error bars were computed from the minimum-maximum of 100 cross-validations (trained on randomly selected 50% of the datasets).

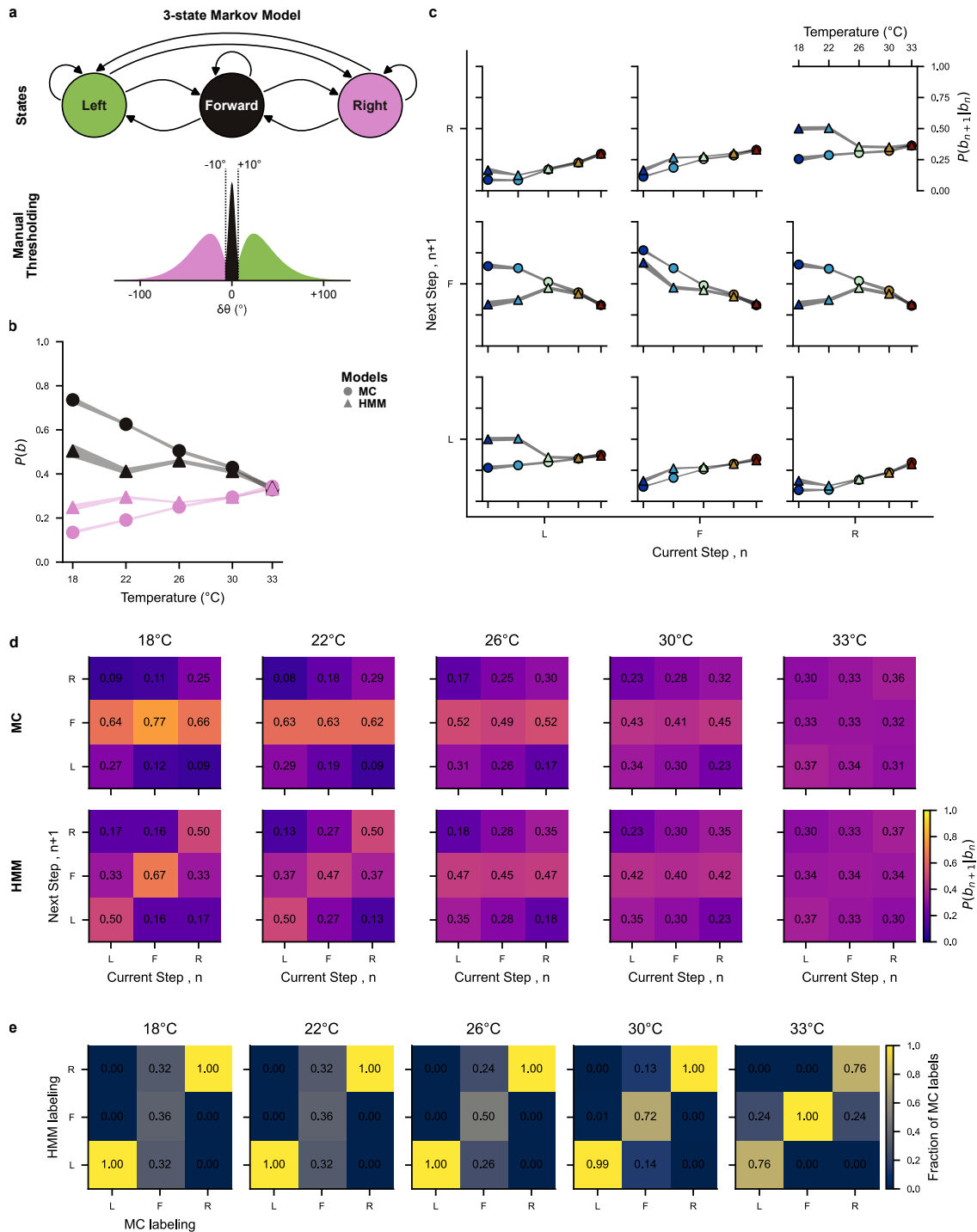


FIG. S3. **Supplementary panels to Fig.2 - Comparison between Markov Chain and Hidden Markov Model:** (a) Diagram illustrating the 3-state Hidden Markov Model (HMM) with emissions modeled as a normal distribution for forward bouts and gamma distributions for turning bouts. (b) Temperature dependence of the steady state bout probabilities $P(s)$ for forward bouts ($s = F$, black) and turning bouts ($s \in L, R$, pink), for both the Markov Chain inferred from thresholded reorientations (MC, circles) and Hidden Markov Models (HMM, triangles). (c) Temperature dependence of the transition probabilities $P(s_n \rightarrow s_{n+1})$ between forward (F), left (L), and right (R) bouts, for both the Markov Chain (MC, circles) and the Hidden Markov Model (HMM, triangles). (b,c) The width of the shaded curves represent the minimum-maximum of 100 cross-validations of both models inferred from randomly selecting 50% of the data. (d) Transition matrices between forward (F), left (L) and right (R) states, for both the Markov chains inferred from thresholded data (MC) and Hidden Markov Model (HMM), and for each temperature. (e) Confusion matrices between labeling of MC and HMM for all temperatures (normalized with respect to the MC labeling).

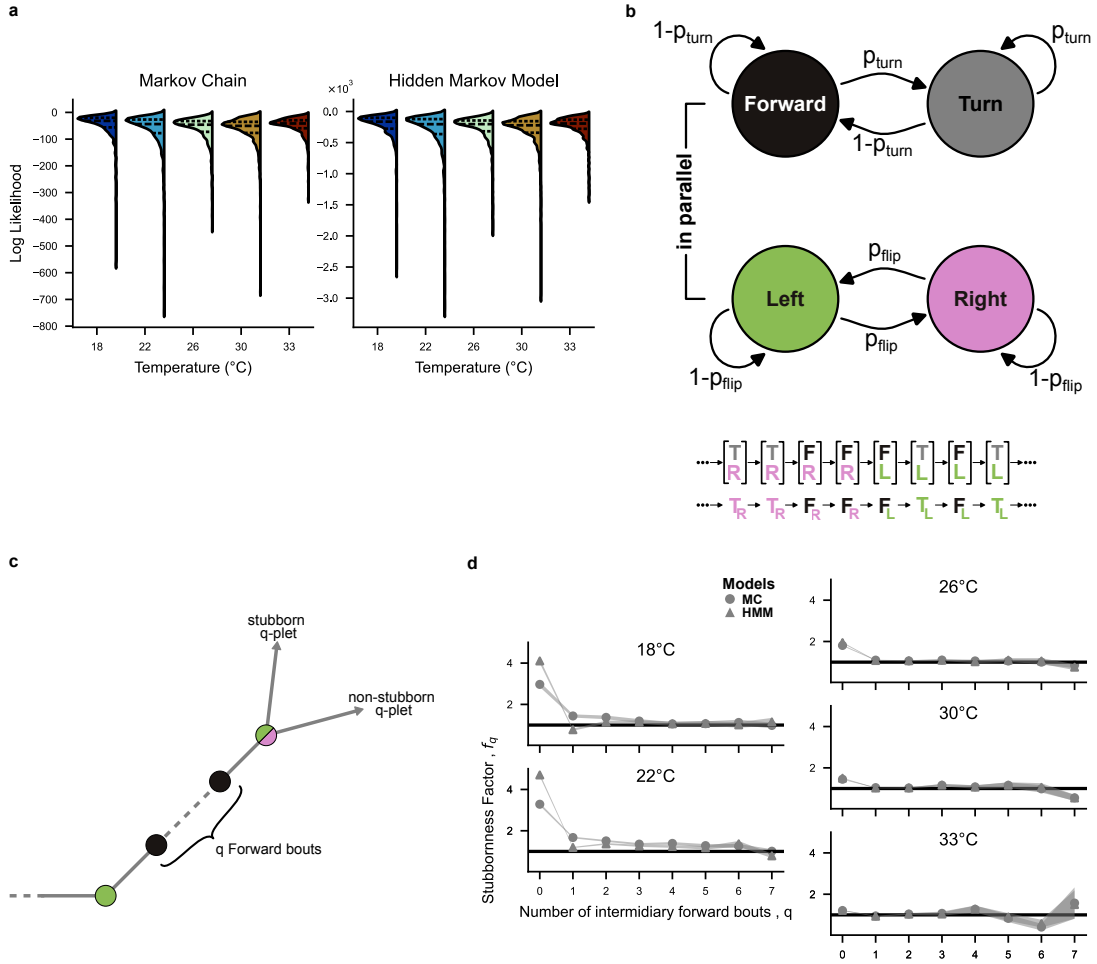


FIG. S4. **Supplementary panels to Fig. 2 - Markovianity:** (a) Distribution of log Likelihoods (LLHs) for both the Markov chains inferred from thresholded data (left) and Hidden Markov Model (right). For each model and each temperature, LLHs were computed for 100 models inferred from 50% of the trajectories (randomly constructed training set) and on the remaining 50% of the trajectories (testing set). Dashed lines show the quartiles of each distribution. (b) Diagram of the 4-state Markov chain used in previous publications [20, 22]. Two Markov Chains run in parallel, with the first chain controlling bout type (forward or turn) and the second controlling direction (left or right). With this model, the system can be in one of four states: $[T, L]$, $[T, R]$, $[F, L]$, $[F, R]$, thus left and right states represent internal directional states (not only observed behavioral orientations). (c) Diagram illustrating the definition of the stubbornness. For a q -plet of bouts $T_1 \rightarrow F \rightarrow \dots \rightarrow F \rightarrow T_2$ with q intermediary forward bouts, a stubborn sequence is defined as one where directionality is conserved (i.e. $T_1 = T_2$), whilst a non-stubborn sequence will lose the memory of the initial turn (i.e. $T_1 \neq T_2$). (d) Evolution of the stubbornness factor f_q (see Eq. 3) with the number of intermediary forward bouts q , comparing the Markov Chain inferred from thresholded trajectories (MC, dots) and the Hidden Markov Model (HMM, triangles) trained directly from reorientation angles, for each temperature. The width of the shaded curves represent the estimated error in *stubbornness* factor (see Materials and Methods IV D).

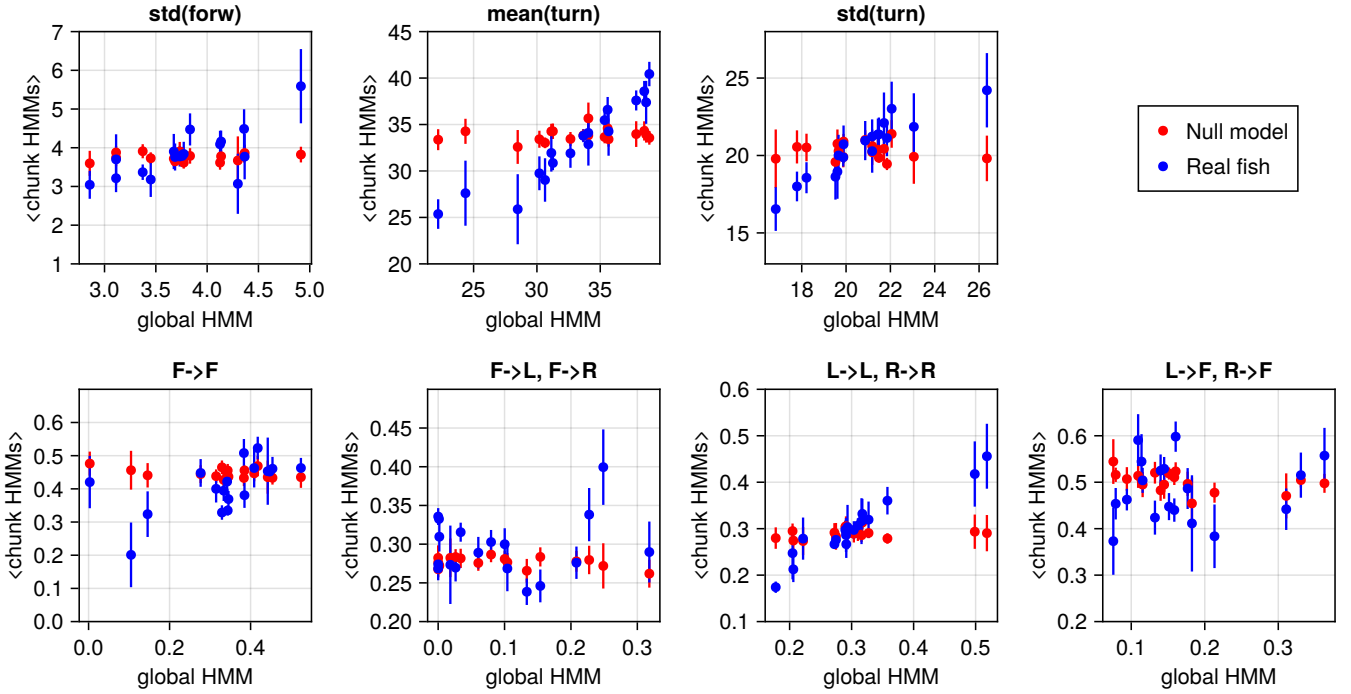


FIG. S5. **Supplementary panels to Fig.3** Hidden Markov Model parameters inferred from all trajectories from an individual fish, compared with the average parameters inferred from chunks of that fish’s trajectories. All HMM parameters are shown. Each dot represents a fish, with error bars corresponding to standard error of the mean. Blue color corresponds to real individual fish data. Red points are obtained by sampling long trajectories from a single HMM trained on all fish bundled together, thus representing a null model for the fish individuality.

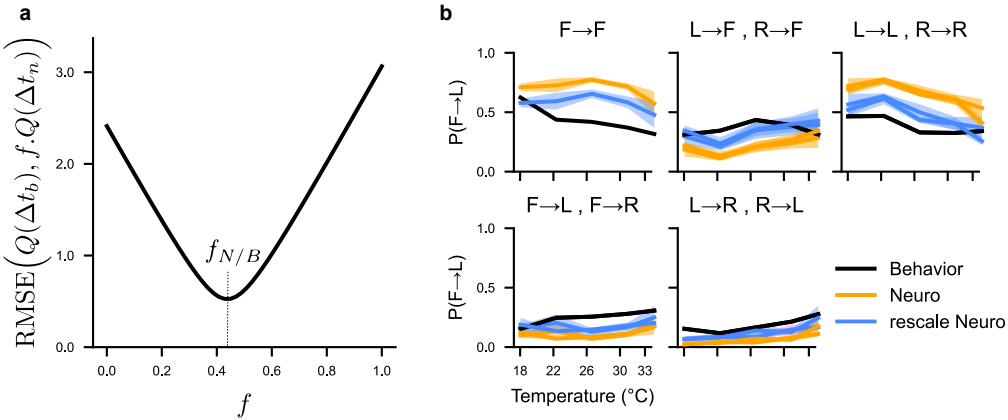


FIG. S6. **Supplementary panels to Fig.5** (a) Root Mean Squared Error (RMSE) between quantiles of the behavior and neuronal sojourn distributions presented in Figure 5a at different values of the rescaling factor f . The optimal rescaling factor corresponds the minimal RMSE at $f = f_{N/B} \approx 0.44$. (b) Comparison of the transition probabilities $P(s \rightarrow s')$ between hidden states F , L , and R , for the behavioral HMM (black), neuronal HMMs (orange), and neuronal HMM rescaled by $f_{N/B} = 0.44$ (magenta) at all 5 recorded temperatures. Shaded curves represent the standard error of the mean for all recorded fish at each temperature.

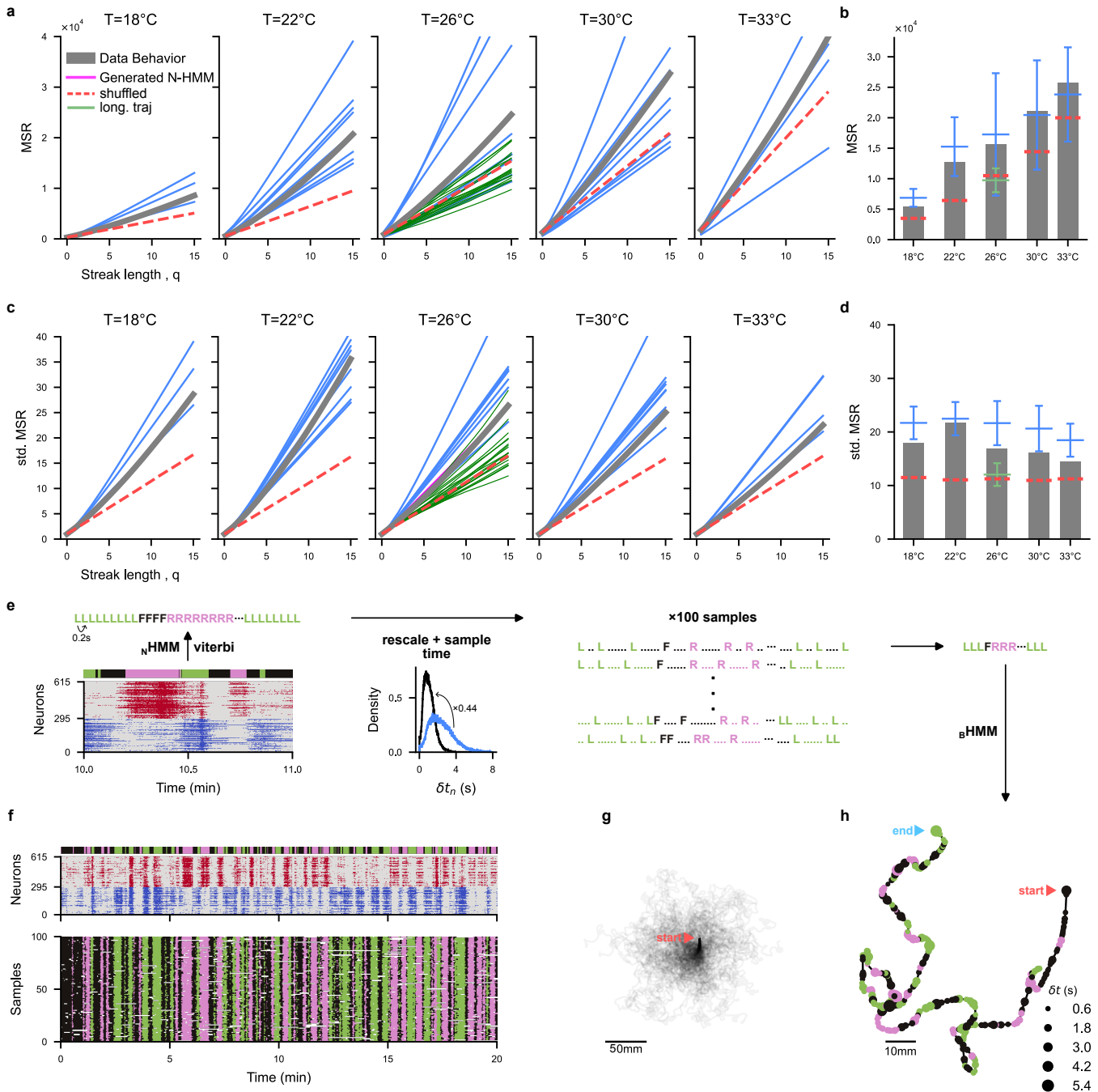


FIG. S7. Supplementary panels to Fig. 6 (a) Mean Square Reorientation (MSR) after q bouts from aggregated multiple-fish trajectories at $18\text{--}33^{\circ}\text{C}$ (grey), long-individual trajectories at 26°C (green) and generated trajectories from Neural HMM (N-HMM) (blue). Red dashed lines are MSR obtained from shuffled aggregated multiple-fish trajectories. (b) Bar plots for the MSR ($q=10$) for data and N-HMM generated trajectories, with mean (horizontal bars) and standard deviations (vertical bars). (c-d) Same as panels a-b but plotting the standardized MSR where trajectories are normalized such that the bout angles have unit variance. See Eq. (A.28). (e) Diagram explaining the conversion from neuronal activity to swim trajectory. ARTR activity is first converted into a sequence of forward, left, right hidden states using the Viterbi algorithm on the N-HMM. Time is then re-scaled using the scaling factor identified in Fig 5, and bout sequences are sampled based on the interbout interval distribution. A swim trajectory is constructed for each bout sequence by sampling the bout distances d_n and inter-bout intervals δt_n emission distributions in the behavioral HMM. (f) Example recorded ARTR activity at 26°C (top) and corresponding state sequences after temporal re-scaling and bout sampling (bottom). (g) Reconstructed trajectories for each sampled state sequence in panel f. (h) Example reconstructed trajectory from the ARTR activity in panel f.